

A nonlinear subgrid-scale model for large-eddy simulations of rotating turbulent flows

Maurits H. Silvis^{*,1}, H. Jane Bae^{†,2}, F. Xavier Trias³, Mahdi Abkar^{‡,2} and Roel Verstappen¹

¹*Bernoulli Institute for Mathematics, Computer Science and Artificial Intelligence, University of Groningen, Nijenborgh 9, 9747 AG Groningen, The Netherlands*

²*Center for Turbulence Research, Stanford University, Stanford, California 94305, USA*

³*Heat and Mass Transfer Technological Center, Technical University of Catalonia, C/ Colom 11, 08222 Terrassa (Barcelona), Spain*

April 30, 2019

Abstract Rotating turbulent flows form a challenging test case for large-eddy simulation (LES). We, therefore, propose and validate a new subgrid-scale (SGS) model for such flows. The proposed SGS model consists of a dissipative eddy viscosity term as well as a nondissipative term that is nonlinear in the rate-of-strain and rate-of-rotation tensors. The two corresponding model coefficients are a function of the vortex stretching magnitude. Therefore, the model is consistent with many physical and mathematical properties of the Navier–Stokes equations and turbulent stresses, and is easy to implement. We determine the two model constants using a nondynamic procedure that takes into account the interaction between the model terms. Using detailed direct numerical simulations (DNSs) and LESs of rotating decaying turbulence and spanwise-rotating plane-channel flow, we reveal that the two model terms respectively account for dissipation and backscatter of energy, and that the nonlinear term improves predictions of the Reynolds stress anisotropy near solid walls. We also show that the new SGS model provides good predictions of rotating decaying turbulence and leads to outstanding predictions of spanwise-rotating plane-channel flow over a large range of rotation rates for both fine and coarse grid resolutions. Moreover, the new nonlinear model performs as well as the dynamic Smagorinsky and scaled anisotropic minimum-dissipation models in LESs of rotating decaying turbulence and outperforms these models in LESs of spanwise-rotating plane-channel flow, without requiring (dynamic) adaptation or near-wall damping of the model constants.

Keywords rotating turbulence, turbulence simulation, turbulence modeling

1 Introduction

Turbulent flows that are subject to solid body rotation are ubiquitous in geophysics, astrophysics and engineering. Consider, for example, flows in the oceans, in the atmosphere or in turbomachinery. Understanding and being able to predict the behavior of such rotating turbulent flows, thus, is of great importance for many applications.

Over the past decades, the fundamental understanding of rotating turbulent flows has grown significantly. Both experimental (Hopfinger et al. 1982; Jacquin et al. 1990; Morize et al. 2005; Staplehurst et al. 2008) and numerical (Bardina et al. 1985; Yeung and Zhou 1998; Smith and Waleffe

*Email address: m.h.silvis@rug.nl

†Current address: Graduate Aerospace Laboratories, California Institute of Technology, Pasadena, California 91125, USA

‡Current address: Department of Engineering, Aarhus University, Inge Lehmanns Gade 10, 8000 Aarhus C, Denmark

1999; Mininni et al. 2009; Thiele and Müller 2009; Bourouiba et al. 2012; Sen et al. 2012) studies of flows far from solid boundaries have revealed very marked effects of rotation on turbulence. Under the influence of rotation, large-scale columnar vortices develop that are aligned with the rotation axis. In addition, the dissipation rate of turbulent kinetic energy reduces and the energy spectrum changes. These effects are caused by the Coriolis force, which modifies the energy transfer in turbulent flows (Bardina et al. 1985; Jacquin et al. 1990; Cambon et al. 1997; Yeung and Zhou 1998; Smith and Waleffe 1999; Chen et al. 2005; Morize et al. 2005; Bourouiba and Bartello 2007; Staplehurst et al. 2008; Mininni et al. 2009; Thiele and Müller 2009; Bourouiba et al. 2012; Sen et al. 2012; Buzzicotti et al. 2018). (Also refer to the reviews by Godeferd and Moisy 2015; Alexakis and Biferale 2018; Sagaut and Cambon 2018, and the references therein.)

Additional interesting effects have been observed in wall-bounded rotating flows. Experiments (Johnston et al. 1972; Nakabayashi and Kitoh 2005) and numerical simulations (Tafti and Vanka 1991; Kristoffersen and Andersson 1993; Lamballais et al. 1996; Grundestam et al. 2008; Yang and Wu 2012; Dai et al. 2016; Xia et al. 2016; Brethouwer 2017) of spanwise-rotating channel flow have shown that the Coriolis force can both enhance and suppress turbulence. On one side of a spanwise-rotating channel, rotation reduces the turbulence intensity and may cause flow laminarization. On the other side of the channel, turbulence will either be enhanced or suppressed, depending on the rotation rate, and large-scale streamwise Taylor–Görtler vortices may occur. The mean streamwise velocity of spanwise-rotating channel flow contains a characteristic linear region. The slope of this region is proportional to the rotation rate, as can be explained using symmetry analysis (Oberlack 2001). As the rotation rate increases, the Coriolis force will suppress turbulence in a growing part of the channel, until the flow fully laminarizes (Grundestam et al. 2008; Xia et al. 2016; Brethouwer 2017). Laminar behavior may, however, be disturbed with intermittent turbulent bursts (Brethouwer et al. 2014; Brethouwer 2016).

Despite the increased fundamental understanding of rotating turbulent flows, the prediction of such flows remains a challenge. This is mainly because many practical rotating flows contain a large range of physically relevant scales of motion, which cannot currently be resolved using direct numerical simulations (DNSs). With the aim to improve the numerical prediction of incompressible rotating turbulent flows, we will, therefore, turn to large-eddy simulation (LES).

In LES, the large scales of motion in a flow are explicitly computed, whereas the effects of the small-scale motions are modeled using subgrid-scale (SGS) models (see, e.g., the monographs by Sagaut 2006; Pope 2011). Eddy viscosity models are commonly used SGS models. These SGS models prescribe the net dissipation of kinetic energy caused by small-scale turbulent motions. The Smagorinsky model (Smagorinsky 1963) and its dynamic variant (Germano et al. 1991; Lilly 1992) are, without a doubt, the most well-known eddy viscosity models. Examples of other, more recently developed eddy viscosity models are the WALE model (Nicoud and Ducros 1999), Vreman’s model (Vreman 2004), the σ model (Nicoud et al. 2011), the QR model (Verstappen et al. 2010; Verstappen 2011; Verstappen et al. 2014), the S3PQR models (Trias et al. 2015), the anisotropic minimum-dissipation model (Rozema et al. 2015), the scaled anisotropic minimum-dissipation model (Verstappen 2018) and the vortex-stretching-based eddy viscosity model (Silvis et al. 2017b; Silvis and Verstappen 2018).

Although eddy viscosity models are effective in many cases, they have an important drawback. They model turbulence as a dissipative process. Given the importance of energy transfer in rotating turbulent flows, it seems unlikely that eddy viscosity models are always suitable for LESs of such flows. More generally, it has since long been known that the rate-of-strain tensor, which forms the basis of eddy viscosity models, does not correlate well with the turbulent stresses (Clark et al. 1979; Bardina et al. 1983; Liu et al. 1994; Tao et al. 2002; Horiuti 2003).

Bardina et al. (1983), therefore, proposed their well-known scale similarity model, in which the largest unresolved motions are modeled in terms of the smallest resolved motions. A related SGS model, often referred to as the gradient model, was proposed by Leonard (1975) and Clark et al. (1979). Both SGS models show a high level of correlation with the turbulent stresses, but do not

provide enough dissipation (Clark et al. 1979; Bardina et al. 1983; Liu et al. 1994; Tao et al. 2002; Horiuti 2003). This motivated the introduction of mixed models, in which the scale similarity or gradient models were combined with an eddy viscosity model (Bardina et al. 1983; Clark et al. 1979; Liu et al. 1994). (More recent support of mixed SGS models is provided by Carati et al. 2001; Tao et al. 2002) Mixed models with a dynamic eddy viscosity term were also considered and were shown to perform well in simulations of different nonrotating flows (Zang et al. 1993; Vreman et al. 1994a, 1996, 1997; Winckelmans et al. 2001).

Lund and Novikov (1992) generalized the gradient model of Leonard (1975) and Clark et al. (1979). They derived a general SGS model consisting of five terms, of which one term was linear and the other terms were nonlinear in the rate-of-strain and rate-of-rotation tensors. Determination of the model constants and coefficients, however, turned out to be a challenging problem. Kosović (1997) proposed a nonlinear SGS model consisting of three terms and determined the model constants using properties of homogeneous isotropic turbulence. Wang and Bergstrom (2005) proposed a dynamic nonlinear SGS model based on the same three model terms. Wendling and Oberlack (2007) investigated dynamic models consisting of different combinations of the five model terms of Lund and Novikov (1992). Kosović (1997), Wang and Bergstrom (2005), and Wendling and Oberlack (2007) successfully applied their SGS models to nonrotating turbulent flows.

SGS models that are nonlinear in the rate-of-strain and rate-of-rotation tensors have also been used in LESs of rotating turbulent flows. Using the terms of Lund and Novikov (1992) as basis tensors, Liu et al. (2004), Yang et al. (2012a), Yang et al. (2012b) and Huang et al. (2017) proposed different nonlinear models for rotating turbulent flows. These authors, however, only validated their SGS models in a very limited number of tests. Moreover, the dynamic procedures proposed by Yang et al. (2012a) and Yang et al. (2012b) are not valid for arbitrary, complex geometries. These procedures additionally rely on the assumption that the eddy viscosity and nonlinear terms of their SGS models do not interact with each other. We will show that this assumption is invalid. Marstorp et al. (2009) proposed a dynamic and a nondynamic nonlinear SGS model based on the transport equation for the Reynolds stress anisotropy. They tested these SGS models in LESs of rotating and nonrotating channel flow, and found that their (dynamic) model outperformed the (dynamic) Smagorinsky model. However, the nonlinear SGS models of Marstorp et al. (2009) require setting four empirical constants, for which no universal values have been found thus far (see, e.g., Marstorp et al. 2009; Montecchia et al. 2017).

As far as we are aware, currently no SGS model for rotating turbulent flows (i) accounts for both dissipation and backscatter of energy; (ii) takes into account the interplay between these processes; (iii) is valid for complex geometries; (iv) can function without near-wall damping functions and dynamic procedures; (v) provides good predictions of different types of rotating turbulent flows over different regimes of rotation; and (vi) works well at both fine and coarse spatial resolutions. Building upon our previous work (Silvis et al. 2016; Silvis and Verstappen 2019), we will, therefore, propose and validate a new SGS model for LESs of incompressible rotating turbulent flows.

First, in Section 2, we discuss the equations underlying LES of rotating turbulent flows and we introduce our notation. Then, in Section 3, we introduce a general class of SGS models based on the velocity gradient. We use this general class of models to propose a new SGS model for rotating turbulent flows in Section 4. In Section 5, we study and validate this SGS model using detailed DNSs and LESs of the two canonical rotating turbulent flows discussed above, namely, rotating decaying turbulence and spanwise-rotating plane-channel flow. We also provide a comparison with the commonly used dynamic Smagorinsky model, the scaled anisotropic minimum-dissipation model and the vortex-stretching-based eddy viscosity model. We present our conclusions in Section 6.

As we will show, both rotating decaying turbulence and spanwise-rotating plane-channel flow form a challenging test case for the considered eddy viscosity models. The proposed SGS model will, on the other hand, provide outstanding predictions of these flows by accounting for both dissipation and backscatter of energy, and by improving predictions of the Reynolds stress anisotropy near solid walls.

2 LES of rotating turbulent flows

We aim to improve the numerical prediction of incompressible rotating turbulent flows using LES. In this section, we discuss the equations underlying LES of rotating flows and we introduce our notation.

2.1 The incompressible Navier–Stokes equations

The behavior of incompressible rotating turbulent flows can be described by the incompressible Navier–Stokes equations in a rotating frame of reference (Grundestam et al. 2008; Pope 2011),

$$\frac{\partial u_i}{\partial t} + \frac{\partial}{\partial x_j}(u_i u_j) = -\frac{1}{\rho} \frac{\partial p}{\partial x_i} + 2\nu \frac{\partial}{\partial x_j} S_{ij}(u) - 2\epsilon_{ijk} \Omega_j u_k, \quad \frac{\partial u_i}{\partial x_i} = 0. \quad (1)$$

Here, u_i represents the velocity field of the flow in the rotating frame (with $i = 1, 2, 3$), while p indicates the pressure. The centrifugal force is absorbed in the pressure. The velocity and pressure are both functions of time t and the three spatial coordinates x_i . The density and kinematic viscosity are labeled ρ and ν , respectively. These quantities are assumed to be constant in time, uniform in space and independent of temperature.

The rate-of-strain tensor $S_{ij}(u)$ is given by the symmetric part of the velocity gradient, i.e.,

$$S_{ij}(u) = \frac{1}{2} \left(\frac{\partial u_i}{\partial x_j} + \frac{\partial u_j}{\partial x_i} \right). \quad (2)$$

Similarly, the rate-of-rotation tensor, which we will use extensively later, is expressed as the antisymmetric part of the velocity gradient,

$$W_{ij}(u) = \frac{1}{2} \left(\frac{\partial u_i}{\partial x_j} - \frac{\partial u_j}{\partial x_i} \right). \quad (3)$$

Since we consider flows within a rotating frame of reference, $W_{ij}(u)$ equals the so-called intrinsic or absolute rotation tensor.

The Coriolis force term is characterized by the rotation rate of the frame of reference, which we label as Ω_i . In the current study, we will consider rotations about the x_3 -axis, i.e., $\Omega_i = \delta_{i3} \Omega_3$, where δ_{ij} represents the Kronecker delta. Moreover, we consider only constant frame rotations. We, thus, take a constant Ω_3 and the Euler, or angular acceleration, force is not included in Eq. (1). The tensor ϵ_{ijk} denotes the Levi-Civita symbol. The Einstein summation convention is assumed throughout for repeated indices, unless otherwise indicated.

2.2 The filtered incompressible Navier–Stokes equations

We will employ LES to predict the large-scale behavior of incompressible rotating turbulent flows. In LES, the behavior of the large scales of motion in a flow is explicitly computed, whereas small-scale effects are modeled. Large and small scales of motion are generally distinguished using a spatial filtering or coarse-graining operation (Leonard 1975; Sagaut 2006). This operation will be indicated by an overbar and is assumed to commute with differentiation. A filter length, which we will denote by $\bar{\delta}$, is associated with filtering.

Filtering the incompressible Navier–Stokes equations of Eq. (1), we obtain the filtered incompressible Navier–Stokes equations in a rotating frame of reference,

$$\frac{\partial \bar{u}_i}{\partial t} + \frac{\partial}{\partial x_j}(\bar{u}_i \bar{u}_j) = -\frac{1}{\rho} \frac{\partial \bar{p}}{\partial x_i} + 2\nu \frac{\partial}{\partial x_j} S_{ij}(\bar{u}) - 2\epsilon_{ijk} \Omega_j \bar{u}_k - \frac{\partial}{\partial x_j} \tau_{ij}(u), \quad \frac{\partial \bar{u}_i}{\partial x_i} = 0. \quad (4)$$

Here, \bar{u}_i and \bar{p} respectively represent the filtered velocity and pressure fields in the rotating frame. The turbulent, or subfilter-scale, stress tensor

$$\tau_{ij}(u) = \bar{u}_i \bar{u}_j - \bar{u}_i \bar{u}_j \quad (5)$$

represents the interactions between large and small scales of motion. Since the turbulent stress tensor is not solely expressed in terms of the large-scale velocity field \bar{u}_i , Eq. (4) is not closed and cannot be solved. We have to model $\tau_{ij}(u)$ to solve this closure problem.

2.3 LES without explicit filtering

We will consider modeling of the turbulent stresses within the context of LES without explicit filtering. That is, we look for closure models $\tau_{ij}^{\text{mod}}(v)$ for the turbulent stress tensor $\tau_{ij}(u)$ of Eq. (5), such that the set of equations given by

$$\frac{\partial v_i}{\partial t} + \frac{\partial}{\partial x_j}(v_i v_j) = -\frac{1}{\rho} \frac{\partial q}{\partial x_i} + 2\nu \frac{\partial}{\partial x_j} S_{ij}(v) - 2\epsilon_{ijk} \Omega_j v_k - \frac{\partial}{\partial x_j} \tau_{ij}^{\text{mod}}(v), \quad \frac{\partial v_i}{\partial x_i} = 0 \quad (6)$$

provides accurate approximations of the large-scale velocity and pressure. In other words, we aim to choose the closure model $\tau_{ij}^{\text{mod}}(v)$ in such a way that $v_i \approx \bar{u}_i$ and $q \approx \bar{p}$.

We will refer to Eq. (6) as the LES equations. The resemblance between Eq. (1) and Eq. (6) reveals that a practical LES without explicit filtering consist in numerically solving the Navier–Stokes equations of Eq. (1) on a coarse grid, supplemented by an extra forcing term to represent any unresolved SGS physics. We will accordingly call the closure model $\tau_{ij}^{\text{mod}}(v)$ a SGS (stress) model. For brevity, we will write

$$\tau_{ij} = \tau_{ij}(u), \quad \tau_{ij}^{\text{mod}} = \tau_{ij}^{\text{mod}}(v), \quad S_{ij} = S_{ij}(v), \quad W_{ij} = W_{ij}(v) \quad (7)$$

in what follows.

3 SGS models based on the local velocity gradient

In this section, we discuss SGS models of eddy viscosity type as well as their limitations. Aiming to go beyond these limitations, we introduce a general class of SGS models based on the local velocity gradient.

3.1 Eddy viscosity models

Eddy viscosity models are SGS models that are based on the Boussinesq hypothesis, which is the assumption that small-scale turbulent motions effectively cause diffusion of the large scales of motion. These SGS models can be expressed as

$$\tau_{ij}^{\text{mod,dev}} = -2\nu_e S_{ij}. \quad (8)$$

Here, the label ‘dev’ indicates the deviatoric part of a tensor, i.e.,

$$\tau_{ij}^{\text{dev}} = \tau_{ij} - \frac{1}{3} \tau_{kk} \delta_{ij}. \quad (9)$$

The eddy viscosity ν_e is commonly defined as a nonlinear function of the velocity gradient. Nonetheless, eddy viscosity models are often called linear models because the eddy viscosity ν_e can be seen as the proportionality constant in the linear relation between the SGS stresses and the rate-of-strain tensor. We will follow this naming convention here and contrast (linear) eddy viscosity models with nonlinear SGS models.

Given their basis in the Boussinesq hypothesis, eddy viscosity models are dissipative SGS models. The dissipative description of turbulent flows they provide is known to work well for decaying homogeneous isotropic turbulence (Lund and Novikov 1992). The Boussinesq hypothesis is, however, known to be invalid in general. Indeed, the SGS stress tensor τ_{ij} is usually not aligned with the

rate-of-strain tensor S_{ij} (Clark et al. 1979; Bardina et al. 1983; Liu et al. 1994; Tao et al. 2002; Horiuti 2003). Therefore, the small scales in a turbulent flow must also have a nondissipative effect on the large scales of motion. As a consequence, we can expect that eddy viscosity models do not provide accurate predictions of all turbulent flows. With their associated energy transfer processes, especially rotating turbulent flows can be expected to form a challenging test case for eddy viscosity models.

3.2 A general class of SGS models

To allow for the description of nondissipative processes in turbulent flows, we consider SGS models that contain tensor terms that are nonlinear in the local velocity gradient. A general class of such models is given by (Rivlin 1955; Spencer and Rivlin 1958, 1962; Pope 1975; Lund and Novikov 1992)

$$\tau_{ij}^{\text{mod}} = \sum_{k=0}^{10} \alpha_{(k)} T_{ij}^{(k)}. \quad (10)$$

Here, the tensors $T_{ij}^{(k)}$ are defined as

$$\begin{aligned} T_{ij}^{(0)} &= \delta_{ij}, & T_{ij}^{(6)} &= S_{ik}W_{kl}W_{lj} + W_{ik}W_{kl}S_{lj}, \\ T_{ij}^{(1)} &= S_{ij}, & T_{ij}^{(7)} &= W_{ik}S_{kl}W_{lm}W_{mj} - W_{ik}W_{kl}S_{lm}W_{mj}, \\ T_{ij}^{(2)} &= S_{ik}S_{kj}, & T_{ij}^{(8)} &= S_{ik}W_{kl}S_{lm}S_{mj} - S_{ik}S_{kl}W_{lm}S_{mj}, \\ T_{ij}^{(3)} &= W_{ik}W_{kj}, & T_{ij}^{(9)} &= S_{ik}S_{kl}W_{lm}W_{mj} + W_{ik}W_{kl}S_{lm}S_{mj}, \\ T_{ij}^{(4)} &= S_{ik}W_{kj} - W_{ik}S_{kj}, & T_{ij}^{(10)} &= W_{ik}S_{kl}S_{lm}W_{mn}W_{nj} \\ T_{ij}^{(5)} &= S_{ik}S_{kl}W_{lj} - W_{ik}S_{kl}S_{lj}, & & - W_{ik}W_{kl}S_{lm}S_{mn}W_{nj}, \end{aligned} \quad (11)$$

and the model coefficients $\alpha_{(i)}$ are generally expressed as

$$\alpha_{(i)} = C_{(i)} \delta^2 f_{(i)}(I_1, I_2, \dots, I_6), \quad (12)$$

where no summation is implied over indices in brackets. Each of the model coefficients consists of three factors: a dimensionless constant $C_{(i)}$; the square of the subgrid characteristic scale δ , which is usually associated with the grid resolution or the LES filter length $\bar{\delta}$; and a function $f_{(i)}$ of the local velocity gradient. By isotropy, each function $f_{(i)}$ can depend only on the combined invariants of the rate-of-strain and rate-of-rotation tensors (Spencer and Rivlin 1962; Pope 1975; Lund and Novikov 1992),

$$\begin{aligned} I_1 &= S_{ij}S_{ji}, & I_3 &= S_{ij}S_{jk}S_{ki}, & I_5 &= S_{ij}S_{jk}W_{kl}W_{li}, \\ I_2 &= W_{ij}W_{ji}, & I_4 &= S_{ij}W_{jk}W_{ki}, & I_6 &= S_{ij}S_{jk}W_{kl}W_{lm}S_{mn}W_{ni}. \end{aligned} \quad (13)$$

Since the tensors of Eq. (11) are symmetric 3×3 matrices, no more than six of them can be linearly independent (Rivlin and Ericksen 1955; Lund and Novikov 1992). Therefore, not all the $T_{ij}^{(k)}$ provide an independent contribution to the sum of Eq. (10). The six tensors $T_{ij}^{(0)}$ to $T_{ij}^{(5)}$ in general suffice to form a linearly independent basis for the turbulent stresses. Only in case of an axisymmetric strain (Lund and Novikov 1992) or when the vorticity vector is aligned with one of the principal directions of strain will a few of these tensors become linearly dependent. In the former case, $T_{ij}^{(6)}$ and $T_{ij}^{(7)}$ may be added as linearly independent basis tensors (Silvis and Verstappen n.d.). Tensors $T_{ij}^{(8)}$ to $T_{ij}^{(10)}$ never contain additional independent information.

Disregarding the exceptional case of an axisymmetric strain (Lund and Novikov 1992), we can express the general class of SGS models of Eq. (10) as

$$\tau_{ij}^{\text{mod}} = \sum_{k=0}^5 \alpha_{(k)} T_{ij}^{(k)}. \quad (14)$$

This general class of SGS models has a basis of six tensors, out of which four are nonlinear in the rate-of-strain and rate-of-rotation tensors. If one is only interested in modeling the deviatoric part of the SGS stresses, as is commonly done for incompressible turbulent flows, one can consider the traceless version of Eq. (14).

The general class of SGS models of Eq. (14) has several appealing properties. First, Eq. (14) is consistent with several symmetries and the known conservation laws of the Navier–Stokes equations. Indeed, Eq. (14) is based on the local velocity gradient and, therefore, automatically satisfies time translation invariance, pressure translation invariance, (generalized) Galilean invariance, and invariance under instantaneous rotations and reflections of the coordinate system (Oberlack 1997; Silvis et al. 2017b; Silvis and Verstappen n.d.). Furthermore, we expressed SGS effects in the LES equations, Eq. (6), in conservative form. The class of SGS models of Eq. (14), therefore, respects the conservation laws of mass, momentum, angular momentum, vorticity and a hierarchy of vorticity-related quantities (Cheviakov and Oberlack 2014; Silvis et al. 2017a; Silvis and Verstappen n.d.). Being based on the absolute rotation tensor W_{ij} , Eq. (14) is also invariant under arbitrary time-dependent rotations of the coordinate system. This property, which is commonly referred to as (three-dimensional) material frame indifference, is not desirable for a turbulence model (Silvis and Verstappen n.d.). However, as long as we are considering rotating turbulent flows from a rotating frame of reference, the definition of Eq. (14) in terms of the absolute rotation tensor does not form a restriction.

Secondly, one can obtain different existing SGS models from Eq. (14) for specific choices of the model coefficients $\alpha_{(i)}$. For example, one recovers the eddy viscosity models of Eq. (8) by setting $\alpha_{(1)} = -2\nu_e$ and $\alpha_{(i)} = 0$ for $i \neq 1$. Also the gradient model of Leonard (1975) and Clark et al. (1979), the general nonlinear model of Lund and Novikov (1992), the SGS model of Kosović (1997), and the explicit algebraic SGS stress model of Marstorp et al. (2009) form specific cases of Eq. (14) (Silvis et al. 2017b).

Finally, the class of SGS models of Eq. (14) can describe dissipative as well as nondissipative processes. Indeed, some terms of Eq. (14) provide a nonzero contribution to the so-called subgrid dissipation (or production of SGS kinetic energy),

$$D^{\text{mod}} = -\tau_{ij}^{\text{mod}} S_{ij}, \quad (15)$$

while other terms are perpendicular to the rate-of-strain tensor. These latter terms, thus, do not directly contribute to the subgrid dissipation and have to describe nondissipative processes.

The general class of SGS models of Eq. (14), therefore, forms a very useful starting point for the construction of new SGS models, which can potentially take us beyond the limitations of eddy viscosity models discussed in Section 3.1. To obtain a practical SGS model from Eq. (14), however, we need to overcome two challenges. First, six terms is too much for a practical and tractable SGS model. We, therefore, have to make a selection of tensor terms from the general formulation of Eq. (14). Secondly, for each tensor term we need to specify a model coefficient $\alpha_{(i)}$. These model coefficients can, however, depend in many dimensionally consistent ways on the combined invariants of the rate-of-strain and rate-of-rotation tensors given in Eq. (13). We, therefore, need a procedure to specify the model coefficients $\alpha_{(i)}$ of each tensor term.

4 A new nonlinear SGS model

In the current section we use the general class of SGS models of Section 3 to propose a new SGS model for rotating turbulent flows. We first select the basis tensors for this new model from Eq. (11).

4.1 Selecting the tensor terms

In practical, coarse-grid LESs of turbulent flows, we do not resolve all the small-scale motions. As a consequence, the kinetic energy in such simulations is dissipated at a smaller rate than expected. A SGS model, therefore, requires a dissipative component. Since dissipation of kinetic energy is naturally modeled using eddy viscosity models, we will select the rate-of-strain tensor $T_{ij}^{(1)} = S_{ij}$ as our first basis tensor.

As mentioned in Section 3.1, the SGS stresses are usually not aligned with the rate-of-strain tensor. Therefore, it is necessary to select a second basis tensor from Eq. (11) that is not fully aligned with the rate-of-strain tensor. In fact, it would be optimal to choose a term that is perpendicular to the rate-of-strain tensor in order to have two terms that can describe distinct physical phenomena. Since we focus on the simulation of rotating turbulent flows, it would also be beneficial if the second tensor term includes the rate-of-rotation tensor.

The simplest tensor of Eq. (11) that is perpendicular to the rate-of-strain tensor and includes the rate-of-rotation tensor is $T_{ij}^{(4)} = S_{ik}W_{kj} - W_{ik}S_{kj}$. This nonlinear tensor has several attractive properties. First of all, $T_{ij}^{(4)}$ does not directly contribute to the subgrid dissipation D^{mod} defined in Eq. (15). Therefore, $T_{ij}^{(4)}$ is a nondissipative tensor that can describe fundamentally different physical phenomena than the rate-of-strain tensor. In fact, the nondissipative and quadratic nature of $T_{ij}^{(4)}$ suggests that this term can model energy transfer in turbulent flows. Secondly, $T_{ij}^{(4)} = S_{ik}W_{kj} - W_{ik}S_{kj}$ involves the rate-of-rotation tensor. We can, therefore, expect that this tensor is very suitable for the simulation of rotating flows. Finally, $T_{ij}^{(4)}$ is part of the gradient model of Leonard (1975) and Clark et al. (1979). More specifically, $T_{ij}^{(4)}$ forms a nondissipative, stable part of the gradient model. The gradient model forms the lowest-order Taylor approximation of the turbulent stress tensor τ_{ij} of Eq. (5) in terms of the filter length $\bar{\delta}$. As such, $T_{ij}^{(4)}$ is consistent with a nondissipative part of the true turbulent stress tensor.

The nonlinear tensor $T_{ij}^{(4)}$ is not only interesting from a theoretical, but also from a practical point of view. Marstorp et al. (2009) showed that addition of a term involving this nonlinear tensor to an eddy viscosity model can significantly improve predictions of the Reynolds stress anisotropy in rotating and nonrotating turbulent channel flow. Follow-up research by Rasam et al. (2011) and Montecchia et al. (2017) furthermore indicates that such a model also performs well at coarse resolutions, in contrast to the dynamic Smagorinsky model (Germano et al. 1991; Lilly 1992). We have also previously obtained promising results from LESs of rotating flows with nonlinear SGS models involving $T_{ij}^{(4)}$ (Silvis et al. 2016; Silvis and Verstappen 2019).

Given the above, we select $T_{ij}^{(4)} = S_{ik}W_{kj} - W_{ik}S_{kj}$ as the second and final basis tensor for our new SGS model for rotating turbulent flows. We, thus, reduce the general class of SGS models of Eq. (14) to the two-term class of models consisting of a dissipative linear eddy viscosity term and a nondissipative nonlinear model term given by

$$\tau_{ij}^{\text{mod,dev}} = \alpha_{(1)}T_{ij}^{(1)} + \alpha_{(4)}T_{ij}^{(4)} = \alpha_{(1)}S_{ij} + \alpha_{(4)}(S_{ik}W_{kj} - W_{ik}S_{kj}). \quad (16)$$

4.2 Defining the model coefficients

We now focus on defining the two model coefficients $\alpha_{(1)}$ and $\alpha_{(4)}$. Specifically, we will define the functions $f_{(1)}$ and $f_{(4)}$ that are part of these model coefficients (see Eq. (12)). Since the functions $f_{(i)}$ can depend in many dimensionally consistent ways on the combined invariants of the rate-of-strain and rate-of-rotation tensors of Eq. (13), we need a procedure to define these functions.

We propose to define the functions $f_{(1)}$ and $f_{(4)}$ that are part of the model coefficients $\alpha_{(1)}$ and $\alpha_{(4)}$ by applying a previously devised framework of constraints for the assessment and creation of SGS models (Silvis et al. 2017a,b; Silvis and Verstappen 2018, n.d.). This framework is based on

the idea that SGS models should be consistent with the fundamental physical and mathematical properties of the Navier–Stokes equations and the turbulent stresses. Specifically, consistency of SGS models with the symmetries (Speziale 1985; Oberlack 1997, 2002; Razafindralandy et al. 2007) and conservation laws (Cheviakov and Oberlack 2014) of the Navier–Stokes equations, and the dissipation properties (Vreman 2004; Razafindralandy et al. 2007; Nicoud et al. 2011; Verstappen 2011), realizability (Vreman et al. 1994b) and near-wall scaling behavior (Chapman and Kuhn 1986) of the turbulent stresses is desired.

As explained in Section 3.2, the general class of SGS models of Eq. (14) by construction satisfies some symmetries and respects the known conservation laws of the Navier–Stokes equations. The two-term class of SGS models of Eq. (16) inherits this desirable behavior. Invariance with respect to scaling transformations of time and space can only be satisfied if we choose a subgrid characteristic length scale that is directly related to flow quantities or if a dynamic procedure (Germano et al. 1991) is used to determine the model constants (Oberlack 1997; Razafindralandy et al. 2007). As we explain in Section 4.3, we take a grid-dependent rather than a flow-dependent characteristic length scale and we determine model constants in a nondynamic way. While this facilitates the model implementation, scaling invariance will be violated. In addition, for traceless SGS models such as the class of SGS models of Eq. (16), we cannot determine if realizability is satisfied (Vreman et al. 1994a; Silvis et al. 2017b).

We can use the remaining properties of the incompressible Navier–Stokes equations and the turbulent stresses to define the model coefficients of Eq. (16). Specifically, the Navier–Stokes equations provide us with two symmetry constraints. A SGS model ideally breaks time reversal invariance (Carati et al. 2001) and satisfies two-dimensional material frame indifference (Oberlack 1997, 2002; Razafindralandy et al. 2007). Note that this latter property only holds in the limit of a two-component incompressible flow and should not be confused with the notion of three-dimensional material frame indifference, which we briefly discussed in Section 3.2. With respect to the properties of the turbulent stress tensor, we have constraints coming from the near-wall scaling behavior of the turbulent stresses (Chapman and Kuhn 1986), the dissipation requirements of Vreman (2004) and Nicoud et al. (2011), consistency with the second law of thermodynamics (Razafindralandy et al. 2007), and the minimum-dissipation requirement of Verstappen (2011). We will now apply these constraints to define the functions $f_{(1)}$ and $f_{(4)}$ that are part of the model coefficients of the class of SGS models of Eq. (16).

To emphasize that the first term on the right-hand side of Eq. (16) is an eddy viscosity term and represents dissipation, we write

$$\alpha_{(1)} = -2\nu_e \tag{17}$$

in what follows. We will write the coefficient of the nondissipative nonlinear term as

$$\alpha_{(4)} = \mu_e. \tag{18}$$

We will, thus, express the two-term class of SGS models of Eq. (16) as

$$\tau_{ij}^{\text{mod,dev}} = -2\nu_e S_{ij} + \mu_e (S_{ik} W_{kj} - W_{ik} S_{kj}). \tag{19}$$

We first focus on defining the eddy viscosity ν_e . The dissipation properties and near-wall-scaling behavior of the turbulent stress tensor provide useful constraints for this quantity. Vreman (2004) and Nicoud et al. (2011) argue that SGS models should not produce SGS kinetic energy in certain simple flows; otherwise these models could cause unphysical transitions from laminar to turbulent flow states. Nicoud et al. (2011) specifically require that SGS models do not cause dissipation in two-component flows or for the pure axisymmetric strain.

In view of these requirements, a very useful quantity to base the eddy viscosity on is $I_5 - \frac{1}{2}I_1 I_2$ (Silvis et al. 2017b; Silvis and Verstappen 2018, n.d.). This nonnegative quantity vanishes in all two-component flows, as well as in states of pure shear and pure rotation. Additionally, this quantity vanishes near solid walls. Indeed, while the invariants I_1, I_2, I_5 all attain constant finite values near a wall, $I_5 - \frac{1}{2}I_1 I_2$

scales as $\mathcal{O}(x_i^2)$ in terms of a wall-normal coordinate x_i (Silvis and Verstappen [n.d.](#)). The quantity $I_5 - \frac{1}{2}I_1I_2$ can, therefore, be used to correct the near-wall scaling and dissipation behavior of the Smagorinsky model (Smagorinsky [1963](#)). To that end, we first normalize $I_5 - \frac{1}{2}I_1I_2$ by $-I_1I_2$. The resulting quantity is dimensionless and, as can be inferred from the following equations, takes on values between 0 and 1/2. Secondly, we impose the desired near-wall scaling of $\nu_e = \mathcal{O}(x_i^3)$ for a wall-normal coordinate x_i (Silvis and Verstappen [n.d.](#)). We so obtain the definition of the eddy viscosity given by (Silvis et al. [2017b](#); Silvis and Verstappen [2018](#))

$$\nu_e = (C_\nu\delta)^2\sqrt{2I_1}\left(\frac{I_5 - \frac{1}{2}I_1I_2}{-I_1I_2}\right)^{3/2}. \quad (20)$$

Here, C_ν^2 denotes a positive dimensionless model constant and δ represents the subgrid characteristic length scale. We discuss the values of C_ν and δ in Section [4.3](#).

The quantity $I_5 - \frac{1}{2}I_1I_2$ in Eq. (20) is proportional to the squared magnitude of the vortex stretching $S_{ij}\omega_j$ (Trias et al. [2015](#)), where the vorticity is defined as

$$\omega_i = \epsilon_{ijk}\frac{\partial}{\partial x_j}v_k = -\epsilon_{ijk}W_{jk}. \quad (21)$$

We can, therefore, rewrite the eddy viscosity of Eq. (20) as

$$\nu_e = (C_\nu\delta)^2\frac{1}{2}|S|f_{\text{VS}}^3, \quad (22)$$

where the normalized vortex stretching magnitude is defined by

$$f_{\text{VS}} = \frac{|S\omega|}{|S||\omega|} \quad (23)$$

and the norms in Eqs. (22) and (23) are defined according to

$$\begin{aligned} |S\omega|^2 &= (S_{ij}\omega_j)(S_{ik}\omega_k) = 4(I_5 - \frac{1}{2}I_1I_2), \\ |S|^2 &= S_{ij}S_{ij} = I_1, \\ |\omega|^2 &= \omega_i\omega_i = 2W_{ij}W_{ij} = -2I_2. \end{aligned} \quad (24)$$

By the Cauchy–Schwarz inequality, the vortex stretching magnitude of Eq. (23) is bounded from below and above: $0 \leq f_{\text{VS}} \leq 1$. We previously termed an eddy viscosity model with the eddy viscosity of Eqs. (20) and (22) the vortex-stretching-based eddy viscosity model (Silvis et al. [2017b](#)).

Since the nonlinear tensor $S_{ik}W_{kj} - W_{ik}S_{kj}$ of Eq. (19) is nondissipative, the above-mentioned dissipation requirements cannot be applied to define μ_e . However, it makes sense to demand that the entire SGS model vanishes in simple flows. We additionally have a desired near-wall scaling behavior of $\mu_e = \mathcal{O}(x_i^4)$ for a wall-normal coordinate x_i (Silvis and Verstappen [n.d.](#)). We will, therefore, also define the model coefficient μ_e in terms of the normalized vortex stretching magnitude f_{VS} of Eq. (23):

$$\mu_e = C_\mu\delta^2\left(\frac{I_5 - \frac{1}{2}I_1I_2}{-I_1I_2}\right)^2 = C_\mu\delta^2\frac{1}{4}f_{\text{VS}}^4. \quad (25)$$

Here, C_μ denotes a dimensionless constant that can take on both positive and negative values. We discuss the values of C_μ and δ in Section [4.3](#).

Combining the expression of the two-term class of SGS models of Eq. (19) with the eddy viscosity ν_e of Eq. (22), the nonlinear model coefficient μ_e of Eq. (25) and the normalized vortex stretching magnitude f_{VS} of Eq. (23), we obtain the full expression of our new SGS model:

$$\tau_{ij}^{\text{mod,dev}} = -2(C_\nu\delta)^2\frac{1}{2}|S|\left(\frac{|S\omega|}{|S||\omega|}\right)^3 S_{ij} + C_\mu\delta^2\frac{1}{4}\left(\frac{|S\omega|}{|S||\omega|}\right)^4 (S_{ik}W_{kj} - W_{ik}S_{kj}). \quad (26)$$

Given the dependence on the vortex stretching magnitude, we will refer to this model as the vortex-stretching-based nonlinear model.

The vortex-stretching-based nonlinear model by construction has several desirable properties. First of all, this SGS model is consistent with many physical and mathematical properties of the Navier–Stokes equations and the turbulent stresses. Indeed, the vortex-stretching-based nonlinear model preserves most of the symmetries of the Navier–Stokes equations, including two-dimensional material frame indifference, and conserves mass, momentum, angular momentum, vorticity and a hierarchy of vorticity-related quantities. Additionally, the eddy viscosity of this SGS model is nonnegative. Thereby, time reversal invariance is broken, as desired, and consistency with the second law of thermodynamics is enforced. Also, the form of the eddy viscosity satisfies the minimum-dissipation requirement of Verstappen (2011) for all flows but the axisymmetric strain. The full vortex-stretching-based nonlinear model vanishes in two-component flows, as well as in other simple flows like purely rotational and pure shear flows. Moreover, this SGS model has the correct scaling behavior near solid walls. The vortex-stretching-based nonlinear model, thus, respects fundamental properties of turbulent flows and is valid for arbitrary, complex flow configurations without requiring near-wall damping functions or dynamic procedures.

Secondly, the two terms of the vortex-stretching-based nonlinear model represent different physical phenomena. The eddy viscosity term describes dissipation of kinetic energy, while the nonlinear term is perpendicular to the rate-of-strain tensor and is consistent with a nondissipative part of the turbulent stress tensor. The nonlinear term can, therefore, represent nondissipative processes in turbulent flows and can help us go beyond the limitations of eddy viscosity models.

4.3 Implementing the new SGS model

The vortex-stretching-based nonlinear model of Eq. (26) can only be used in practice once the two model constants and the subgrid characteristic length scale are defined. To determine the desired order of magnitude of the model constants, we first assume that they can be set independently.

Ignoring the nonlinear term, we can estimate the constant C_ν of the eddy viscosity term of Eq. (26) using a simple dissipation argument. We require that the average subgrid dissipation due to the eddy viscosity term matches the average dissipation of the Smagorinsky model in (nonrotating) homogeneous isotropic turbulence (Nicoud and Ducros 1999; Nicoud et al. 2011; Trias et al. 2015). We estimate the average subgrid dissipation of the eddy viscosity term and the Smagorinsky model using a large number of synthetic velocity gradients, given by traceless random matrices (Nicoud et al. 2011; Trias et al. 2015) sampled from a uniform distribution (Silvis et al. 2017b). We then equate the two averages to obtain an estimate of the model constant C_ν . A set of MATLAB scripts that can perform this estimation of the constants of eddy viscosity models has been made freely available.¹ We obtain

$$C_\nu^2 = 0.3373 \approx 0.34 \quad (27)$$

for a Smagorinsky constant of 0.17. We previously showed that good predictions of decaying homogeneous isotropic turbulence and plane-channel flow can be obtained using the eddy viscosity term of Eq. (26) with a model constant close to the value of Eq. (27) (Silvis et al. 2017a,b).

Since the nonlinear term of the vortex-stretching-based nonlinear model of Eq. (26) is nondissipative, the model constant C_μ cannot be determined using the above dissipation estimate. Moreover, since SGS models at least have to capture the net dissipation of kinetic energy that characterizes turbulence, the nonlinear term cannot be used as a standalone SGS model. If we assume that the dissipation of kinetic energy is accounted for, we can, however, determine the desired order of magnitude of C_μ . To that end, we compare the average value of the coefficient of the nonlinear term $S_{ik}W_{kj} - W_{ik}S_{kj}$ of

¹ See <https://github.com/mauritssilvis/lesTools> for a set of MATLAB scripts that can be used to estimate the model constants of subgrid-scale models for large-eddy simulation.

Eq. (26) with the proportionality constant of the same nonlinear term in the gradient model of Leonard (1975) and Clark et al. (1979). The average value of the coefficient of the nonlinear term of Eq. (26) is determined using a large number of synthetic velocity gradients with the previously mentioned set of MATLAB scripts.² Comparing the resulting average with the proportionality constant of 1/12 of the gradient model, we expect that the constant of the nonlinear term has to be of the order of

$$C_\mu \sim 2.0 - 2.5. \quad (28)$$

Although the two terms of the vortex-stretching-based nonlinear model represent different physics, they are not dynamically independent of each other. Indeed, as we will see in Section 5.1.3, the eddy viscosity term modulates the effects of the nonlinear term. Also, the nonlinear term will have an (indirect) effect on the dissipation of kinetic energy. Therefore, the two model constants of the vortex-stretching-based nonlinear model cannot be set independently and we have to modify the values given by Eqs. (27) and (28). In Section 5.1.3, we will propose a nondynamic method to determine the model constants that takes into account the interplay between the two model terms. This method leads to

$$C_\nu^2 = 0.1687 \approx 0.17, \quad C_\mu = 5. \quad (29)$$

We discuss the physical interpretation of these values in Sections 5.1.3 and 5.1.4.

We also have to define the subgrid characteristic length scale δ of the vortex-stretching-based nonlinear model of Eq. (26). For simplicity, we will assume that the different physical processes that are described by the two terms of this model can be characterized using the same length scale. For ease of implementation we will define this length scale in terms of the grid spacings. Specifically, we take Deardorff’s classical definition for the subgrid characteristic length scale (Deardorff 1970),

$$\delta = (\Delta x_1 \Delta x_2 \Delta x_3)^{1/3}. \quad (30)$$

Here, the Δx_i represent the dimensions of the local grid cell.

As can be inferred from Eqs. (26) and (30), the vortex-stretching-based nonlinear model only relies on two quantities, namely, the velocity gradient and the grid cell sizes. Both quantities are normally available in numerical simulations of turbulent flows. The vortex-stretching-based nonlinear model, therefore, is easy to implement. In addition, most of the constituents of the nonlinear term follow from computing the eddy viscosity term. Computing the two terms of Eq. (26), therefore, is only slightly more costly than computation of the eddy viscosity term alone.

To obtain the best results with the vortex-stretching-based nonlinear model of Eq. (26) with the model constants of Eq. (29), we recommend the use of a numerical implementation that preserves the different nature of the two model terms. That is, a dissipative implementation is desired for the eddy viscosity term, while the nonlinear term should conserve kinetic energy. More generally, we recommend the use of a discretization in which the convective and Coriolis force terms of Eq. (6) as well as the nonlinear term of the SGS model conserve kinetic energy. At the same time, the diffusive term of Eq. (6) and the eddy viscosity term of the vortex-stretching-based model should be implemented in such a way that they can only cause (a nonnegative) dissipation of kinetic energy.

5 Numerical results

We will now study in detail the vortex-stretching-based nonlinear model of Eq. (26) using DNSs and LESs of rotating decaying turbulence and spanwise-rotating plane-channel flow. We also compare predictions from this SGS model and the commonly used dynamic Smagorinsky model (Germano et al. 1991; Lilly 1992), the scaled anisotropic minimum-dissipation model (Verstappen 2018) and the vortex-stretching-based eddy viscosity model (Silvis et al. 2017b; Silvis and Verstappen 2018).

² See Footnote 1.

All numerical simulations were performed using incompressible Navier–Stokes solvers employing staggered finite-volume or finite-difference methods of second-order spatial accuracy, based on the discretization of Verstappen and Veldman (2003). This discretization ensures conservation of kinetic energy by the convective and Coriolis force terms as well as a strictly positive dissipation by the diffusive term. To enforce a nonnegative dissipation of kinetic energy by the eddy viscosity term of the vortex-stretching-based nonlinear model and conservation of kinetic energy by the nonlinear term, we discretize these terms according to the work by Remmerswaal (2016). An explicit two-step one-leg time integration scheme of second order accuracy, which is similar to an Adams-Bashforth scheme, is used for the integration of the convective, viscous, Coriolis force and SGS model terms (Verstappen and Veldman 2003). A projection method, which involves solution of a Poisson equation for the pressure, is used to ensure incompressibility of the velocity field (Kim and Moin 1985).

5.1 Rotating decaying turbulence

In the current section, we study the vortex-stretching-based nonlinear model of Eq. (26) using DNSs and LESs of rotating decaying turbulence. Rotating decaying turbulence is a prototypical rotating turbulent flow that allows us to study the effects of rotation on turbulence, without the influence of external forces, walls, etc. With this initial test case, we have three aims. First of all, we want to understand the workings and interplay of the two terms of the vortex-stretching-based nonlinear model. Secondly, we want to determine the values of the model constants of this model. Finally, we want to make a first comparison of this new SGS model with existing SGS models.

5.1.1 Test case

The test case of rotating decaying turbulence used in this work is inspired by the experiments of Comte-Bellot and Corrsin (1971) on nonrotating decaying turbulence. They investigated the properties of decaying (roughly) isotropic turbulence, which was generated by a regular grid in a uniform flow of air. Among other quantities, they measured energy spectra at three different stations downstream of the grid.

We simulate the flow of the experiment by Comte-Bellot and Corrsin inside a triply periodic cubic box with edge length $L_{\text{ref}} = 11M = 55.88$ cm (Rozema et al. 2015; Silvis et al. 2017b). Here, $M = 5.08$ cm represents the mesh size of the turbulence-generating grid. We imagine that the simulation box is moving away from the turbulence-generating grid with the initial mean velocity of the flow of air in the experiment, $U_0 = 1000$ cm s⁻¹. The time in the numerical simulations, thus, corresponds to the distance from the grid in the experiment. In the simulations performed for the current study, we exposed the flow in the box to rotation about the vertical (x_3) axis through addition of the Coriolis force.

The initial conditions of the numerical simulations were designed to have the same energy spectrum as the flow at the first measurement station of the experiment by Comte-Bellot and Corrsin. This was done through the procedure outlined by Rozema et al. (2015), using the MATLAB scripts that these authors made publicly available.³ In the first step of this procedure, an incompressible velocity field with random phases is created (Kwak et al. 1975), which has an energy spectrum that fits the spectrum measured at the first station. Secondly, to adjust the phases, this velocity field is fed into a preliminary numerical simulation. Preliminary simulations on a coarse grid were run with the QR model (Verstappen et al. 2010; Verstappen 2011; Verstappen et al. 2014). Finally, a rescaling operation (Kang et al. 2003) is applied to the velocity field, to again match the energy spectrum of the flow in the first measurement station. For the purposes of the current research, the Coriolis force term was turned on in the preliminary simulations, and the above procedure was repeated for each

³ See <https://github.com/hjbae/CBC> for a set of MATLAB scripts that can be used to generate initial conditions for numerical simulations of homogeneous isotropic turbulence.

rotation rate and spatial resolution investigated below. The resulting velocity fields served as initial conditions for our numerical simulations.

Our test case of rotating decaying turbulence can be characterized using two dimensionless parameters. These are the Reynolds and rotation numbers, respectively given by

$$Re = \frac{u_{\text{ref}} L_{\text{ref}}}{\nu}, \quad Ro = \frac{2\Omega_3 L_{\text{ref}}}{u_{\text{ref}}}. \quad (31)$$

Here, u_{ref} and L_{ref} represent a reference velocity and length scale, respectively. The kinematic viscosity is again denoted by ν . The quantity Ω_3 represents the rotation rate about the vertical (x_3) axis. We take as reference velocity $u_{\text{ref}} = 27.19 \text{ cm s}^{-1}$, which corresponds to the initial root-mean-square turbulence intensity of the flow. That is, at the first station, Comte-Bellot and Corrsin measured a turbulent kinetic energy per unit mass given by $E_{\text{kin}} = 3u_{\text{ref}}^2/2$ (Comte-Bellot and Corrsin 1971). With the previously mentioned reference length scale, $L_{\text{ref}} = 55.88 \text{ cm}$, and the value of the viscosity of air in the experiment, $\nu = 0.15 \text{ cm}^2 \text{ s}^{-1}$, the initial Reynolds number is given by $Re = 10\,129$. In our simulations, we vary the rotation number from $Ro = 0$ (no rotation) to $Ro = 200$ (rapid rotation). Note that the rotation number equals the inverse of the Rossby number, which is also used to characterize rotating flows.

We can alternatively define the Reynolds and rotation numbers of Eq. (31) using the (longitudinal) integral length scale L and the (transverse) Taylor microscale λ . We will denote these dimensionless parameters as Re_L , Re_λ , Ro_L and Ro_λ . The rotation numbers based on the integral length scale and the Taylor microscale give information about the strength of the Coriolis force (Jacquin et al. 1990; Cambon et al. 1997; Bourouiba and Bartello 2007). If $Ro_L < 1$, the rotation is weak and the dynamics of the flow are not affected by the Coriolis force. When, on the other hand, $Ro_L \gtrsim 1$, rotation impacts the large scales of motion. As long as the Taylor-microscale rotation number satisfies $Ro_\lambda < 1$, the small-scale motions are not affected by the Coriolis force. Finally, if $Ro_\lambda \gtrsim 1$, the rotation is rapid. That is, all scales of motion are influenced by rotation and the Coriolis force dominates the convective nonlinear term.

In Sections 5.1.2 to 5.1.4, we discuss results obtained from DNSs and LESs of rotating decaying turbulence. We specifically show three-dimensional energy spectra $E(|k|)$ at time $t \approx 171M/U_0$, which corresponds to the third measurement station of the experiment of Comte-Bellot and Corrsin (1971). The energy spectra are provided per unit mass and in units of $u_{\text{ref}}^2 L_{\text{ref}} / (2\pi)$, and are a function of the magnitude of the wavenumber k , which is given in units of $2\pi/L_{\text{ref}}$. Note that a small wavenumber corresponds to a large-scale motion, while large wavenumbers correspond to small scales of motion. We also report the turbulent kinetic energy per unit mass E_{kin} , defined as

$$E_{\text{kin}} = \int_{k=0}^{\infty} E(|k|) dk. \quad (32)$$

Since integration is limited to a finite wavenumber range in numerical simulations, the quantity E_{kin} computed from a coarse-grid simulation at best represents the resolved turbulent kinetic energy. To allow for a fair comparison between DNSs and LESs, we, therefore, also consider the turbulent kinetic energy up to the grid cutoff of our LESs,

$$E_{\text{kin,C}} = \int_{k=0}^{k_C} E(|k|) dk. \quad (33)$$

Here, k_C represents the wavenumber of the grid cutoff of our LESs. We employ a sharp spectral cutoff filter, so that $E_{\text{kin,C}}$ equals the filtered turbulent kinetic energy. In what follows, the turbulent kinetic energy per unit mass E_{kin} is given in units of $3u_{\text{ref}}^2/2$. The turbulent kinetic energy up to the grid cutoff $E_{\text{kin,C}}$ will be normalized with respect to its initial value. Both variants of the turbulent kinetic energy are shown as a function of nondimensional time tU_0/M .

Table 1: Initial rotation and Reynolds numbers of our direct numerical simulations of rotating decaying turbulence on a 512^3 grid.

Ro	Ro_L	Ro_λ	Re	Re_L	Re_λ
0	0.0	0.00	10 129	367	78
50	2.6	0.55	10 129	367	78
100	5.2	1.10	10 129	367	78
200	10.4	2.21	10 129	367	78

In our numerical simulations of rotating decaying turbulence we employed uniform, isotropic grids with periodic boundary conditions. Using a grid convergence study, we determined that a spatial resolution of 64^3 grid points is most suitable for LESs of this flow. For this grid resolution, around 80% of the initial turbulent kinetic energy of the flow is resolved, which is the percentage that is generally strived for in LESs (Pope 2011). Furthermore, the integral length scale, which forms the characteristic size of the large eddies, can be resolved on this grid. We also found that as much as 99% of the initial turbulent kinetic energy is resolved using a 512^3 grid. With this resolution, the grid size is only 3.5 times larger than the Kolmogorov length, close to the recommended value of 2 (Pope 2011). Moreover, energy spectra obtained from simulations on 256^3 and 512^3 grids practically collapse up to the 128^3 grid cutoff at $k_C L_{\text{ref}}/(2\pi) = 64$. Numerical results obtained using a 512^3 grid, therefore, are accurate enough to reveal the physical behavior of rotating decaying turbulence and to serve as reference data for our LESs.

5.1.2 Physical behavior

To prepare for our LESs, we first discuss the typical physical behavior of rotating decaying turbulence using results from DNSs. We specifically discuss the effects of rotation on the energy spectra and turbulent kinetic energy of rotating decaying turbulence with initial Reynolds number $Re = 10\,129$ and rotation numbers $Ro = 0$ to $Ro = 200$. The results communicated in this section were obtained using a 512^3 grid resolution and were partly reported previously (Silvis et al. 2016).

Table 1 shows the initial physical parameters of our DNSs of rotating decaying turbulence. The rotation numbers based on the integral length scale and Taylor microscale, Ro_L and Ro_λ , show that these simulations probe different regimes of rotation. First, for $Ro = 0$, we have a flow without imposed rotation. Secondly, for $Ro = 50$, rotation affects the large scales of motion (as $Ro_L > 1$), but not the small-scale motions (as $Ro_\lambda < 1$). As the rotation number increases to $Ro = 100$, the small-scale motions may start to be influenced also (as $Ro_\lambda \sim 1$). Finally, for $Ro = 200$, we reach a state of rapid rotation in which all scales of motion are affected by the Coriolis force (as $Ro_\lambda > 1$). The initial Reynolds numbers take on the same value for each rotation rate since we start all simulations from velocity fields with the same energy spectrum.

Figure 1 shows the energy spectra and turbulent kinetic energy computed from our DNSs of rotating decaying turbulence. We see that both $Ro = 50$ and $Ro = 100$ correspond to an intermediate regime of rotation in which the large-scale motions are affected by the Coriolis force, but the small-scale motions are not. For $Ro = 200$, we observe a state of rapid rotation in which all scales of motion are affected by rotation. From Fig. 1 we also clearly see that the dissipation rate of turbulent kinetic energy reduces in turbulence that is subjected to rotation. Moreover, an increase in the rotation number goes along with a characteristic steepening of the energy spectrum.

The reduced dissipation rate of turbulent kinetic energy is a nontrivial effect of the Coriolis force. This force does not appear in the evolution equation of the (turbulent) kinetic energy and, therefore, does not produce nor dissipate (turbulent) kinetic energy. The Coriolis force, however, indirectly reduces the viscous dissipation of turbulent kinetic energy by causing transfer of energy from small to large-scale motions. Rotating turbulent flows can, therefore, be expected to form a challenging test

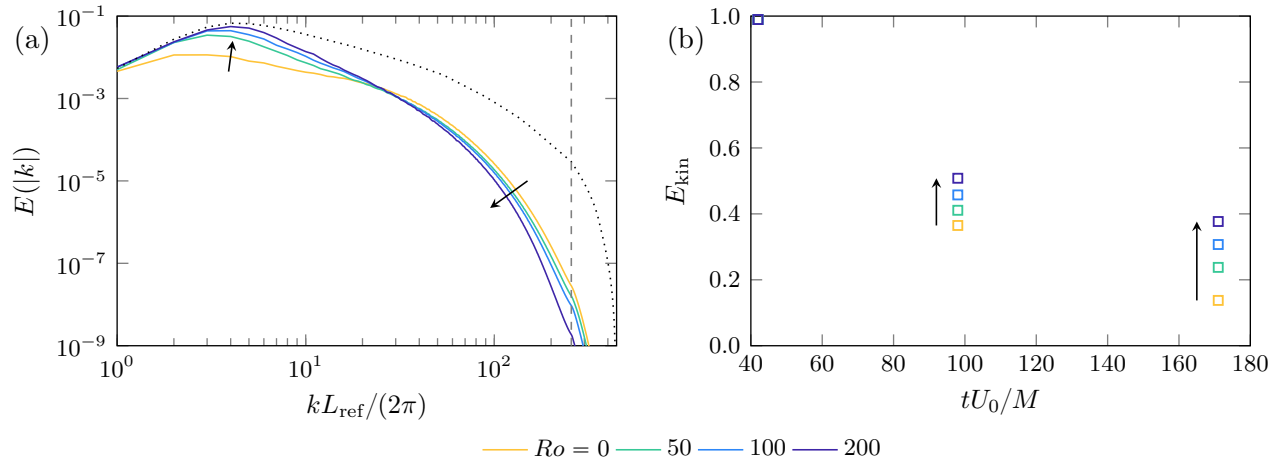


Figure 1: Rotation number dependence of (a) the energy spectrum at time $t \approx 171M/U_0$ and (b) the turbulent kinetic energy of rotating decaying turbulence with initial Reynolds number $Re = 10\,129$. Results were obtained from direct numerical simulations on a 512^3 grid. The dotted line and the vertical dashed line respectively represent the initial energy spectrum and the 512^3 grid cutoff. Arrows indicate the direction of increasing rotation number.

case for dissipative SGS models, such as eddy viscosity models.

5.1.3 Effects of the nonlinear SGS model

In the current section, we study the effects and interplay of the two terms of the vortex-stretching-based nonlinear model of Eq. (26) using LESs of nonrotating and rotating decaying turbulence. We also propose a nondynamic procedure to determine the model constants of this SGS model.

Figure 2 shows predictions of the energy spectrum and turbulent kinetic energy of decaying homogeneous isotropic turbulence with initial Reynolds number $Re = 10\,129$ and rotation number $Ro = 0$. These results were obtained from LESs on a 64^3 grid with the vortex-stretching-based nonlinear model. To determine the effects of the eddy viscosity term, we varied the model constant C_ν from $C_\nu^2 = 0$ to $C_\nu^2 \approx 0.68$ (twice the value suggested in Eq. (27)). Figure 2(a) shows that energy piles up close to the grid cutoff, which is located at $k_C L_{\text{ref}}/(2\pi) = 32$, in the absence of eddy viscosity ($C_\nu^2 = 0$). For $C_\nu^2 \approx 0.68$, which gives rise to a large value of the eddy viscosity, no pile-up of energy occurs. The eddy viscosity term, thus, causes dissipation of turbulent kinetic energy, as expected. We also see that the pile-up of energy that is visible for $C_\nu^2 = 0$ goes along with a depletion of energy of the large and intermediate scales of motion. This depletion is not visible for $C_\nu^2 \approx 0.68$. The eddy viscosity term, thus, has a significant impact on the whole energy spectrum through dissipation.

To determine the effects of the nonlinear term, we varied C_μ from -15 to 15. As Fig. 2(a) shows, the nonlinear model term significantly modulates the energy levels of the large and, especially, of the intermediate scales of motion. We observe either of two effects depending on the sign of the model constant C_μ . For negative C_μ , the nonlinear term causes (additional) forward scatter of kinetic energy from the large and intermediate scales to the grid scale. For positive C_μ , the nonlinear term causes backscatter of energy toward the large scales and/or inhibits the forward energy cascade. The eddy viscosity and nonlinear terms of the vortex-stretching-based nonlinear model, thus, describe distinct physical effects, namely, dissipation and transfer of energy, respectively.

As Fig. 2(a) shows, however, the effects of the nonlinear term reduce as the constant C_ν of the eddy viscosity term grows. The two model terms, thus, interact. This same conclusion can be drawn from Fig. 2(b), which shows that the nonlinear term modulates the dissipation rate of turbulent kinetic energy. Do note that the nonlinear term does not in itself cause dissipation of energy. Rather,

LES (64^3), $Ro = 0$

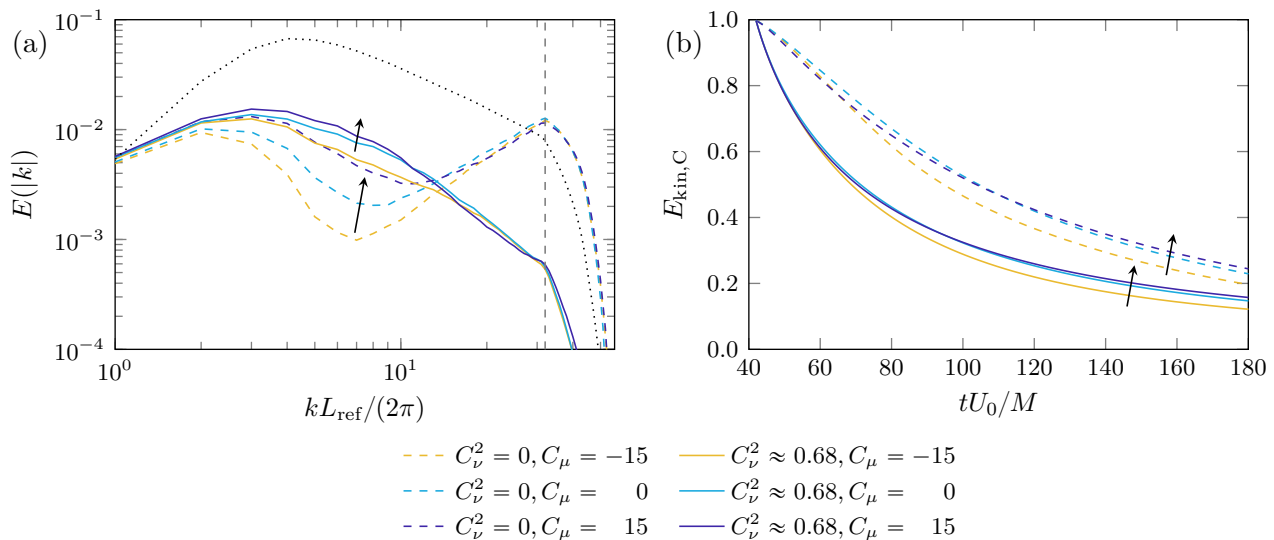


Figure 2: Model constant dependence of predictions of (a) the energy spectrum at time $t \approx 171M/U_0$ and (b) the normalized turbulent kinetic energy up to the 64^3 grid cutoff of decaying homogeneous isotropic turbulence with initial Reynolds number $Re = 10\,129$ and rotation number $Ro = 0$. Results were obtained from large-eddy simulations (LESs) on a 64^3 grid with the vortex-stretching-based nonlinear model with various values of the model constants C_ν and C_μ . The dotted line and the vertical dashed line respectively represent the initial energy spectrum and the 64^3 grid cutoff. Arrows indicate the direction of increasing C_μ .

the nonlinear model term causes energy transfer to or from the smallest resolved scales of motion, whereby this term indirectly influences the dissipation that is most active at those scales. Thus, despite their different nature, the eddy viscosity and nonlinear terms of the vortex-stretching-based nonlinear model are not dynamically independent and the commonly used assumption (see, e.g., Yang et al. 2012a; Yang et al. 2012b) that dissipative eddy viscosity and nondissipative nonlinear terms can be treated independently is invalid. As a consequence, the model constants of the vortex-stretching-based nonlinear model cannot be set independently of each other. Rather, we need to determine C_ν and C_μ such that the interplay between the two model terms is taken into account. To that end, we discuss the behavior of the vortex-stretching-based nonlinear model in rotating decaying turbulence.

Figure 3 shows predictions of the energy spectrum and turbulent kinetic energy of decaying turbulence with initial Reynolds number $Re = 10\,129$ at rotation numbers $Ro = 0$ and 200. These results were obtained from LESs on a 64^3 grid using the vortex-stretching-based nonlinear model with $C_\nu^2 \approx 0.17$ and values of the nonlinear model constant between $C_\mu = -15$ and 15. A smaller value of C_ν is considered for Fig. 3 than for Fig. 2 to be able to study the combined effects of the eddy viscosity term and rotation. Figure 3 shows that the increase in forward (backward) scatter for negative (positive) model constant C_μ also occurs at nonzero rotation numbers. For $Ro = 200$, these effects are, however, much smaller than for $Ro = 0$. Thus, the effects of the nonlinear term reduce both when the eddy viscosity increases and when the rotation number grows. When high rotation rates ($Ro \geq 200$) are combined with large eddy viscosities ($C_\nu^2 > 0.34$), the nonlinear model term turns off entirely.

Using this observation, we can propose a nondynamic method to determine the model constants of the vortex-stretching-based nonlinear model that takes into account the interplay between the two model terms. We first have to determine the value of the model constant C_ν for which the eddy viscosity term provides the correct (reduced) dissipation of turbulent kinetic energy in LESs of rapidly

LES (64^3), $C_\nu^2 \approx 0.17$

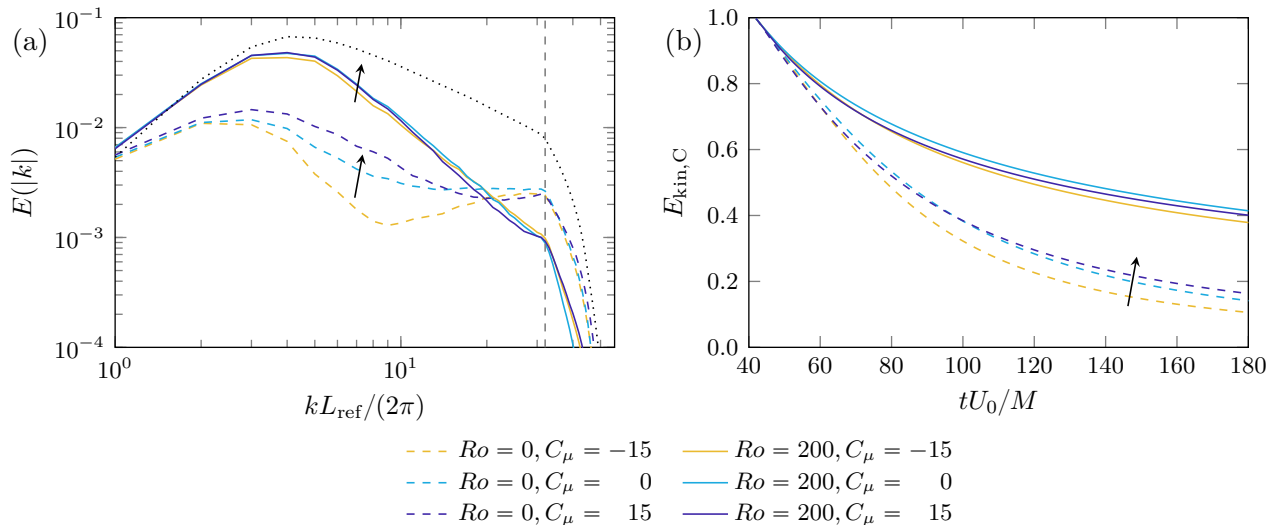


Figure 3: Model constant and rotation number dependence of predictions of (a) the energy spectrum at time $t \approx 171M/U_0$ and (b) the normalized turbulent kinetic energy up to the 64^3 grid cutoff of (rotating) decaying turbulence with initial Reynolds number $Re = 10\,129$. Results were obtained from large-eddy simulations (LESs) on a 64^3 grid with the vortex-stretching-based nonlinear model with $C_\nu^2 \approx 0.17$ and various values of C_μ . The dotted line and the vertical dashed line respectively represent the initial energy spectrum and the 64^3 grid cutoff. Arrows indicate the direction of increasing C_μ .

rotating decaying turbulence. From our DNSs and LESs of rotating decaying turbulence with $Ro = 200$, we found that this is the case for half the value provided in Eq. (27), i.e., $C_\nu^2 = 0.1687 \approx 0.17$. The resulting eddy viscosity term will, however, not dissipate enough turbulent kinetic energy in LESs of decaying turbulence exposed to a lower rotation rate. As a result, forward scatter of energy will deplete the intermediate and/or large scales of motion. To counter this forward scatter of energy, we secondly determine the model constant C_μ for which the nonlinear term provides sufficient backscatter in LESs of rotating decaying turbulence at intermediate rotation rates. From our DNSs and LESs with $Ro = 50$ and 100 we found $C_\mu \approx 5$, which is about twice the value suggested in Eq. (28). The determined values of C_ν and C_μ constitute the model constants of the vortex-stretching-based nonlinear model provided in Eq. (29) of Section 4.3.

5.1.4 LESs of rotating decaying turbulence

We now present a detailed comparison of predictions of rotating decaying turbulence obtained with the vortex-stretching-based nonlinear model and with several eddy viscosity models. We specifically discuss LESs performed with the dynamic Smagorinsky model (Germano et al. 1991; Lilly 1992); the scaled anisotropic minimum-dissipation model (Verstappen 2018) with and without an added nonlinear term; two variants of the vortex-stretching-based eddy viscosity model (Silvis et al. 2017b; Silvis and Verstappen 2018); and the new vortex-stretching-based nonlinear model of Eq. (26). The scaled anisotropic minimum-dissipation model of Verstappen (2018) forms an adaptation of the anisotropic minimum-dissipation model of Rozema et al. (2015). On anisotropic grids these two models provide different results, but they are the same for the isotropic grids used in our LESs of rotating decaying turbulence.

Figures 4 and 5 show predictions of the energy spectrum and turbulent kinetic energy of decaying turbulence with initial Reynolds number $Re = 10\,129$ and rotation numbers $Ro = 0, 100, 200$. These

LES (64^3)

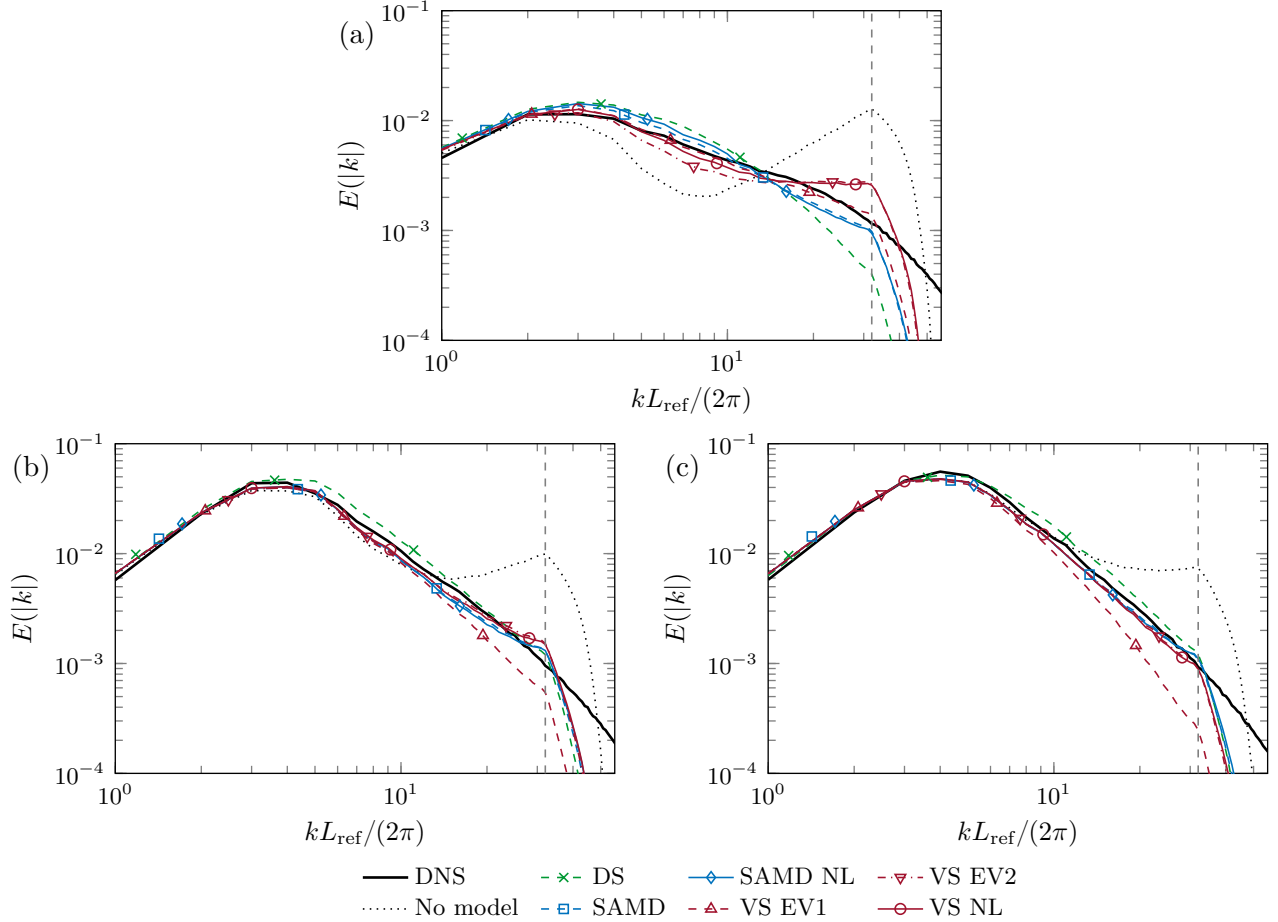


Figure 4: Predictions of the energy spectrum of rotating decaying turbulence with rotation number (a) $Ro = 0$, (b) $Ro = 100$ and (c) $Ro = 200$, and initial Reynolds number $Re = 10129$ at time $t \approx 171M/U_0$. Results were obtained from direct numerical simulations (DNSs) on a 512^3 grid as well as from large-eddy simulations (LESs) on a 64^3 grid without a model, and with the dynamic Smagorinsky model (DS); the scaled anisotropic minimum-dissipation model without (SAMD) and with a nonlinear model term with $C_\mu = 5$ (SAMD NL); the vortex-stretching-based eddy viscosity model with $C_\nu^2 \approx 0.34$ (VS EV1) and $C_\nu^2 \approx 0.17$ (VS EV2); and the vortex-stretching-based nonlinear model with $C_\nu^2 \approx 0.17$ and $C_\mu = 5$ (VS NL). The vertical dashed lines represent the 64^3 grid cutoff.

results were obtained from LESs on a 64^3 grid. We discuss the results contained in Figs. 4 and 5 per SGS model. The energy spectra in Fig. 4 show that the dynamic Smagorinsky model overpredicts the energy content of the large to intermediate scales of motion for all considered rotation numbers. The small-scale energy content is underpredicted in the nonrotating case. Better predictions of the energy content of the small scales of motion are obtained for decaying turbulence subject to rotation. Due to the overprediction of the large-scale kinetic energy, the dynamic Smagorinsky model, however, overpredicts the total turbulent kinetic energy of rotating decaying turbulence (see Fig. 5).

The scaled anisotropic minimum-dissipation model also slightly overpredicts the large-scale and underpredicts the small-scale kinetic energy of nonrotating decaying turbulence (see Fig. 4(a)). In rotating decaying turbulence, the scaled anisotropic minimum-dissipation model tends to underpredict the energy content of the intermediate scales. Apart from some pile-up of energy for $Ro = 100$, the general shape of the spectrum is predicted well by this model, however. If we consider the fact that

LES (64^3)

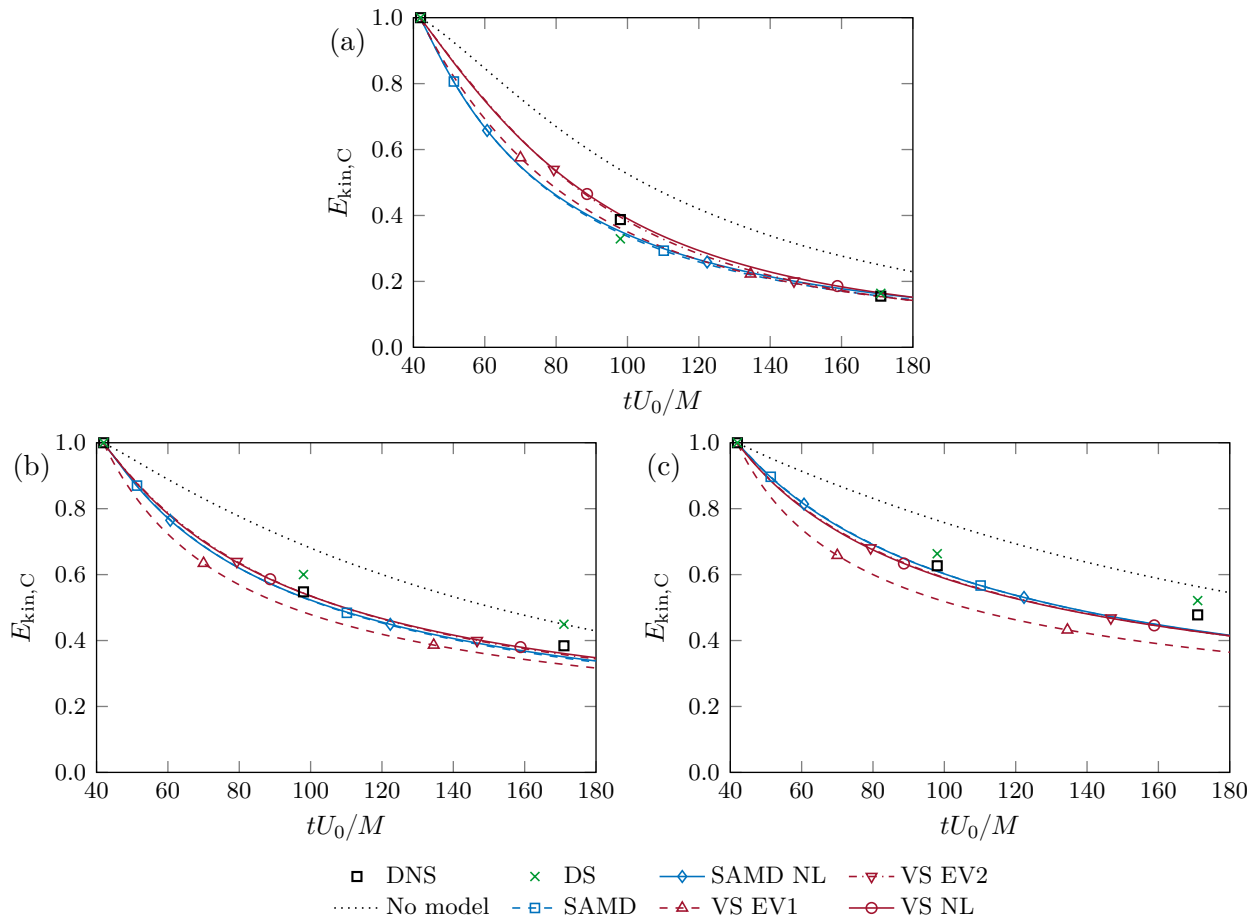


Figure 5: Predictions of the normalized turbulent kinetic energy up to the 64^3 grid cutoff of rotating decaying turbulence with rotation number (a) $Ro = 0$, (b) $Ro = 100$ and (c) $Ro = 200$, and initial Reynolds number $Re = 10\,129$. Results were obtained from direct numerical simulations (DNSs) on a 512^3 grid as well as from large-eddy simulations (LESs) on a 64^3 grid without a model, and with the dynamic Smagorinsky model (DS); the scaled anisotropic minimum-dissipation model without (SAMD) and with a nonlinear model term with $C_\mu = 5$ (SAMD NL); the vortex-stretching-based eddy viscosity model with $C_\nu^2 \approx 0.34$ (VS EV1) and $C_\nu^2 \approx 0.17$ (VS EV2); and the vortex-stretching-based nonlinear model with $C_\nu^2 \approx 0.17$ and $C_\mu = 5$ (VS NL).

the scaled anisotropic minimum-dissipation model is based on a kinetic energy balance (Rozema et al. 2015; Verstappen 2018), which does not include the Coriolis force, this model leads to surprisingly good predictions of rotating decaying turbulence. Adding the nonlinear term of the vortex-stretching-based nonlinear model (with model constant $C_\mu = 5$) to the scaled anisotropic minimum-dissipation model, does not have a significant impact on these predictions. This could be expected, since the above-mentioned kinetic energy balance does not take into account a nonlinear model term that is causing energy transfer.

Figures 4 and 5 also contain predictions from the vortex-stretching-based eddy viscosity models with $C_\nu^2 \approx 0.34$ and $C_\nu^2 \approx 0.17$. For $C_\nu^2 \approx 0.34$, we obtain a very good prediction of the energy spectrum of nonrotating decaying turbulence (see Fig. 4(a)). This was expected, given the dissipation estimate used to determine this model constant. For rotating turbulence, this model is much too dissipative, however, as evidenced by figures 4(b,c) and 5(b,c). On the other hand, the vortex-stretching-based

eddy viscosity model with $C_\nu^2 \approx 0.17$ gives good predictions of rotating decaying turbulence. Indeed, this SGS model only slightly underpredicts the energy of the large and intermediate scales of motion for $Ro = 100$ and 200 , and only leads to some pile-up of energy at the grid scale for $Ro = 100$ (see Fig. 4(b,c)). Expectedly, energy piles up at the grid scale for the nonrotating case, which goes along with the excessive forward scatter of intermediate-scale energy that we discussed in Section 5.1.3. Predicting both rotating and nonrotating decaying turbulence, thus, is challenging for eddy viscosity models.

The vortex-stretching-based nonlinear model (with $C_\nu^2 \approx 0.17$ and $C_\mu = 5$) does not remove the pile-up of energy caused by the vortex-stretching-based eddy viscosity model with $C_\nu^2 \approx 0.17$ in LESs of nonrotating decaying turbulence. More important than avoiding this pile-up of energy, however, is that this model improves the prediction of the intermediate-scale energy content of nonrotating decaying turbulence (refer to Fig. 4(a)). At the same time, this model provides good predictions of the energy spectra of rotating decaying turbulence, as shown in Fig. 4(b,c). By accounting for both dissipation and backscatter of energy, the vortex-stretching-based nonlinear model, thus, provides good predictions of rotating decaying turbulence over different regimes of rotation. Moreover, despite being a nondynamic model, the vortex-stretching-based nonlinear model performs as well as the dynamic Smagorinsky and scaled anisotropic minimum-dissipation models.

5.2 Spanwise-rotating plane-channel flow

We now study in detail the performance of the vortex-stretching-based nonlinear model using DNSs and LESs of a prototypical wall-bounded rotating turbulent flow, namely, spanwise-rotating plane-channel flow. We also compare predictions obtained using this SGS model with predictions from other SGS models.

5.2.1 Test case

A spanwise-rotating plane-channel flow is a plane Poiseuille flow that is subjected to rotation about the spanwise (x_3) axis. Such a flow can be characterized by two dimensionless parameters, namely, the Reynolds and rotation numbers, which we respectively define as

$$Re_\tau = \frac{u_\tau d}{\nu}, \quad Ro_\tau = \frac{2\Omega_3 d}{u_\tau}. \quad (34)$$

Here, u_τ represents the friction velocity and d is the channel half-width. The kinematic viscosity is denoted by ν and the rotation rate about the x_3 -axis is given by Ω_3 . The Coriolis force induces an asymmetry in the flow in a spanwise-rotating plane channel. Therefore, the friction velocity u_τ is defined as

$$u_\tau = \sqrt{\frac{1}{2}(u_\tau^u)^2 + \frac{1}{2}(u_\tau^s)^2}, \quad (35)$$

where u_τ^u and u_τ^s are the friction velocities on the so-called unstable and stable sides of the channel, which are respectively given by

$$u_\tau^u = \sqrt{\nu \left. \frac{d\langle v_1 \rangle}{dx_2} \right|_{x_2=0}}, \quad u_\tau^s = \sqrt{-\nu \left. \frac{d\langle v_1 \rangle}{dx_2} \right|_{x_2=2d}}. \quad (36)$$

Here, v_1 represents the streamwise velocity, the wall-normal coordinate is denoted as x_2 and $\langle \cdot \rangle$ is an average over time as well as over the homogeneous streamwise (x_1) and spanwise (x_3) directions. The friction Reynolds numbers corresponding to the unstable and stable sides of the channel will be denoted by Re_τ^u and Re_τ^s , respectively. Where convenient we will provide distances in terms of the viscous length scales given by the ratio of the viscosity ν and any of the three friction velocities u_τ^u , u_τ^s or u_τ , respectively indicated by the superscripts ‘u’, ‘s’ and ‘c’ (for the channel center), as well as a +.

In our numerical simulations of spanwise-rotating plane-channel flow, we impose a constant pressure gradient in the streamwise (x_1) direction to ensure that $Re_\tau \approx 395$. The rotation number ranges from $Ro_\tau = 0$ (no rotation) to $Ro_\tau = 1000$ (very rapid rotation). As far as we are aware, such a large range of rotation numbers has not previously been considered for this Reynolds number. The flow domain is either given the dimensions $L_1 \times L_2 \times L_3 = 2\pi d \times 2d \times \pi d$ or $L_1 \times L_2 \times L_3 = 3\pi d \times 2d \times \pi d$.

In Sections 5.2.2 to 5.2.5, we study first- and second-order statistics of the velocity field of spanwise-rotating plane-channel flow. We focus in particular on the mean streamwise velocity $\langle v_1 \rangle$ and the Reynolds stresses R_{ij} , which we define as

$$R_{ij} = \langle v_i v_j \rangle - \langle v_i \rangle \langle v_j \rangle. \quad (37)$$

Many commonly used SGS models, including those employed in the current work, are traceless. Traceless SGS models do not incorporate a model for the SGS kinetic energy and can, therefore, only predict the deviatoric part of the Reynolds stresses (Winckelmans et al. 2002), also called the Reynolds stress anisotropy,

$$R_{ij}^{\text{dev}} = R_{ij} - \frac{1}{3} R_{kk} \delta_{ij}. \quad (38)$$

Note that only the diagonal elements of the Reynolds stress anisotropy and Reynolds stress tensors differ. Before a fair comparison can be made between the Reynolds stress (anisotropy) from our DNSs and LESs, the stress (anisotropy) from our LESs, in principle, has to be compensated by the average SGS model contribution (Winckelmans et al. 2002). In LESs of (spanwise-rotating) channel flow, the diagonal elements of eddy viscosity models generally have a magnitude of at most a few percent relative to the Reynolds stress anisotropy. On the other hand, the diagonal elements of the nonlinear model term of Eq. (26) can take on values of the order of the Reynolds stress anisotropy. Compensating the diagonal elements of the Reynolds stress anisotropy by the SGS model contribution, therefore, is not necessary for eddy viscosity models, but is essential when including the nonlinear term. Since the model contribution can be of the order of the Reynolds shear stress for all SGS models, compensation of this stress component is necessary for both eddy viscosity and nonlinear models. In addition to the mean streamwise velocity, we, therefore, report the compensated Reynolds shear stress and compensated Reynolds stress anisotropy where applicable. Below, these quantities are shown in units of the friction velocity u_τ , as indicated by a superscript +.

From the mean streamwise velocity $\langle v_1 \rangle$, we can compute the bulk velocity

$$U_b = \frac{1}{2d} \int_{x_2=0}^{2d} \langle v_1 \rangle \, dx_2. \quad (39)$$

The bulk velocity allows us to define different dimensionless parameters that characterize spanwise-rotating channel flow, namely, the bulk Reynolds and rotation numbers. These numbers can be defined as

$$Re_b = \frac{U_b d}{\nu}, \quad Ro_b = \frac{2\Omega_3 d}{U_b}. \quad (40)$$

We report both the friction-velocity-based dimensionless numbers of Eq. (34) and the bulk-velocity-based numbers of Eq. (40) in what follows.

In our numerical simulations of spanwise-rotating plane-channel flow, we employ periodic boundary conditions in the streamwise (x_1) and spanwise (x_3) directions. We use a uniform grid spacing in these periodic directions, while the grid is stretched in the wall-normal (x_2) direction. The wall-normal coordinates of the grid points in the lower half of the channel ($0 \leq x_2 \leq d$) are defined by

$$x_{2,(j)} = d \frac{\sinh(\gamma j / N_2)}{\sinh(\gamma / 2)} \quad \text{for } j = 0, 1, \dots, N_2/2, \quad (41)$$

where N_2 represents the number of grid points in the wall-normal direction and the stretching parameter γ is given the value 7. The grid points in the upper half of the channel ($d \leq x_2 \leq 2d$) follow from

mirroring the coordinates of Eq. (41) in the channel center. Using a grid convergence study, we found that numerical simulations of spanwise-rotating plane-channel flow with $Re_\tau \approx 395$ and domain sizes $2\pi d \times 2d \times \pi d$ and $3\pi d \times 2d \times \pi d$ could benefit from SGS modeling for spatial resolutions of 32^3 to 64^3 grid points. We also found that first- and second-order velocity field statistics obtained with spatial resolutions between 128^3 and $256 \times 128 \times 256$ grid cells lie very close to each other, verifying the accuracy of these results. We, therefore, use a $256 \times 128 \times 256$ grid for our DNSs of spanwise-rotating plane-channel flow, and resolutions of 32^3 and 64^3 grid points for our LESs, for both domain sizes.

As mentioned in Section 5, we use an explicit scheme for the time integration of the convective, viscous and Coriolis force terms of the Navier–Stokes equations. These terms, therefore, restrict the time step size in our simulations. To ensure stable integration of the convective and viscous terms, we use time steps of at most $\Delta t = 1 \times 10^{-3} d/u_\tau$, $2.5 \times 10^{-4} d/u_\tau$ and $2 \times 10^{-5} d/u_\tau$ for our numerical simulations of nonrotating channel flow on 32^3 , 64^3 and $256 \times 128 \times 256$ grids, respectively. The Coriolis force term has a CFL condition that does not depend on the grid size, but on the rotation rate. We found that time steps of size $\Delta t \lesssim 1/(10Ro_\tau) d/u_\tau$ lead to stable integration of this term. For coarse-grid simulations with a high rotation number, the Coriolis force, thus, restricts the time step more than the convective and viscous forces. To ensure convergence of the mean streamwise velocity and elements of the Reynolds stress (anisotropy), we divide each channel flow simulation into two phases. We first let the turbulence in the channel develop into a statistically steady state. Then we record the average velocity and Reynolds stresses. As we will see in Section 5.2.2, the numerical results presented here have been obtained from sufficiently long runs of statistically steady flows.

In our DNSs of spanwise-rotating plane-channel flow we observed turbulent bursts (Brethouwer et al. 2014; Brethouwer 2016). Turbulent bursts are resonant instabilities that only occur for certain domain sizes, and Reynolds and rotation numbers. We observed turbulent bursts for the rotation numbers $Ro_\tau = 25$ to 100, while these turbulent instabilities do not seem to occur on a $3\pi d \times 2d \times \pi d$ domain. Turbulent bursts last for approximately $3 d/u_\tau$ time units and can be alternated with calmer flow periods of $100 d/u_\tau$ time units. Their magnitude is so large, however, that they lead to large peaks in long-time averages of the Reynolds stresses. We also observed a quasi-periodic collapse of the mean streamwise velocity for several rotation numbers $Ro_\tau \geq 150$ with the domain size $3\pi d \times 2d \times \pi d$, but not for the $2\pi d \times 2d \times \pi d$ domain. In this cyclic process, the mean streamwise velocity drastically reduces and recovers over a period of approximately $300 d/u_\tau$ time units. Each collapse seems to be preceded and caused by a steady growth of turbulence close to the unstable wall of the channel, which is likely due to the quasi-periodic fluctuation of Taylor–Görtler vortices (Dai et al. 2016). Both turbulent bursts and the observed quasi-periodic collapse of the mean streamwise velocity have a large impact on flow statistics that is difficult to predict. Since we want to make a fair comparison between predictions of rotating turbulent flows provided by different SGS models, we had better prevent these turbulent instabilities. We, therefore, choose the domain size $3\pi d \times 2d \times \pi d$ for numerical simulations of spanwise-rotating plane-channel flow with rotation numbers $0 \leq Ro_\tau \leq 100$ and the domain size $2\pi d \times 2d \times \pi d$ for the rotation numbers $125 \leq Ro_\tau \leq 1000$. In coarse-grid simulations on a $2\pi d \times 2d \times \pi d$ domain, turbulent bursts may occur for rotation numbers over $Ro_\tau = 100$. In that case, we also use the $3\pi d \times 2d \times \pi d$ domain.

5.2.2 Physical behavior

To prepare for our LESs, we first discuss the typical physical behavior of spanwise-rotating plane-channel flow using results from DNSs. We specifically discuss the effects of rotation on the first- and second-order statistics of the velocity field of spanwise-rotating plane-channel flow with friction Reynolds number $Re_\tau \approx 395$. The rotation number covers the large range of values from $Ro_\tau = 0$ to $Ro_\tau = 1000$.

Table 2 shows the physical parameters as well as the grid spacings in units of the viscous length scales of our DNSs of spanwise-rotating plane-channel flow. A few important observations can be

Table 2: Rotation and Reynolds numbers, and grid spacings in units of the viscous length scales of our direct numerical simulations of spanwise-rotating plane-channel flow with friction Reynolds number $Re_\tau \approx 395$ on a $256 \times 128 \times 256$ grid. The horizontal rule separates the results with domain size $3\pi d \times 2d \times \pi d$ from those with domain size $2\pi d \times 2d \times \pi d$.

Ro_τ	Ro_b	Re_b	Re_τ	Re_τ^u	Re_τ^s	$\Delta x_1^{u,+}$	$\Delta x_1^{s,+}$	$\Delta x_2^{u,+}$	$\Delta x_2^{c,+}$	$\Delta x_2^{s,+}$	$\Delta x_3^{u,+}$	$\Delta x_3^{s,+}$
0	0	6823	395	395	395	15	15	0.7	21	0.7	5	5
25	0.9	11 509	395	489	269	18	10	0.8	21	0.4	6	3
50	1.2	16 862	395	471	299	17	11	0.8	21	0.5	6	4
75	1.3	22 095	394	454	322	17	12	0.8	21	0.5	6	4
100	1.5	26 857	393	441	338	16	12	0.7	21	0.6	5	4
125	1.6	31 412	395	432	353	11	9	0.7	21	0.6	5	4
150	1.7	35 281	394	424	362	10	9	0.7	21	0.6	5	4
175	1.8	38 724	394	417	370	10	9	0.7	21	0.6	5	5
200	1.9	41 786	395	412	377	10	9	0.7	21	0.6	5	5
225	2.0	44 450	395	408	382	10	9	0.7	21	0.6	5	5
250	2.1	46 681	395	404	386	10	9	0.7	21	0.6	5	5
500	3.8	52 312	396	396	396	10	10	0.7	21	0.7	5	5
1000	7.6	52 313	396	396	396	10	10	0.7	21	0.7	5	5

made from this table. First, the bulk rotation number Ro_b does not vary linearly with the friction rotation number Ro_τ . Specifically, the initial jump in Ro_b seems to indicate that $Ro_\tau = 25$ represents a significant rotation rate. Secondly, the friction Reynolds number corresponding to the unstable wall, Re_τ^u , is larger than Re_τ for most nonzero rotation numbers, while the opposite holds for the friction Reynolds number corresponding to the stable wall, Re_τ^s . The three friction Reynolds numbers are equal for the rotation numbers $Ro_\tau = 500$ and 1000 . Thirdly, all values of the friction Reynolds number Re_τ lie within 0.5 % of 395. This indicates our results have converged in time. The data-taking phase was between 28 and 40 time units of d/u_τ long for each simulation, corresponding to 70 (for $Ro_\tau = 0$) to 600 (for $Ro_\tau = 1000$) channel flow-through times with respect to the bulk velocity U_b . Finally, the values of the grid spacings in units of the viscous length scales show that we have run fine wall-resolved DNSs (Georgiadis et al. 2010).

Figure 6 shows the mean streamwise velocity and Reynolds shear stress computed from our DNSs of spanwise-rotating plane-channel flow. The mean streamwise velocity shown in Fig. 6(a) clearly exhibits a linear region with slope Ro_τ . This linear region is linked to a parabolic part of the velocity profile, which grows as the rotation number increases and indicates (partial) laminarization of the flow (Xia et al. 2016). For the two largest rotation numbers considered here, namely $Ro_\tau = 500$ and 1000 , the entire velocity profile is parabolic. This parabolic profile has a slope of magnitude 395 on both walls of the channel. We can, thus, confirm the hypothesis that full laminarization occurs when the mean streamwise velocity has a slope of $2\Omega_3$ at the wall (Grundestam et al. 2008) or, equivalently, when the friction rotation and Reynolds numbers are equal (Xia et al. 2016).

Also the Reynolds shear stress, provided in Fig. 6(b), shows that the flow in a plane channel laminarizes over a growing region when the spanwise rotation rate increases. We do, however, observe two additional interesting effects. First, the Reynolds shear stress in the lower part of the channel (close to $x_2 = 0$) initially increases in intensity as the rotation number grows and is larger than the shear stress in the nonrotating channel up to $Ro_\tau = 100$. The stress decreases for larger rotation numbers. Secondly, the shear stress in the upper part of the channel (close to $x_2 = 2d$) has already decayed to zero for $Ro_\tau = 25$. This rotation number, therefore, indeed represents a significant rotation rate. These results are consistent with previous observations at other friction Reynolds numbers (Grundestam et al. 2008; Xia et al. 2016; Brethouwer 2017) and we adopt the existing terminology (Johnston et al. 1972; Grundestam et al. 2008; Yang and Wu 2012; Brethouwer 2017) of ‘unstable’ and ‘stable’ sides of

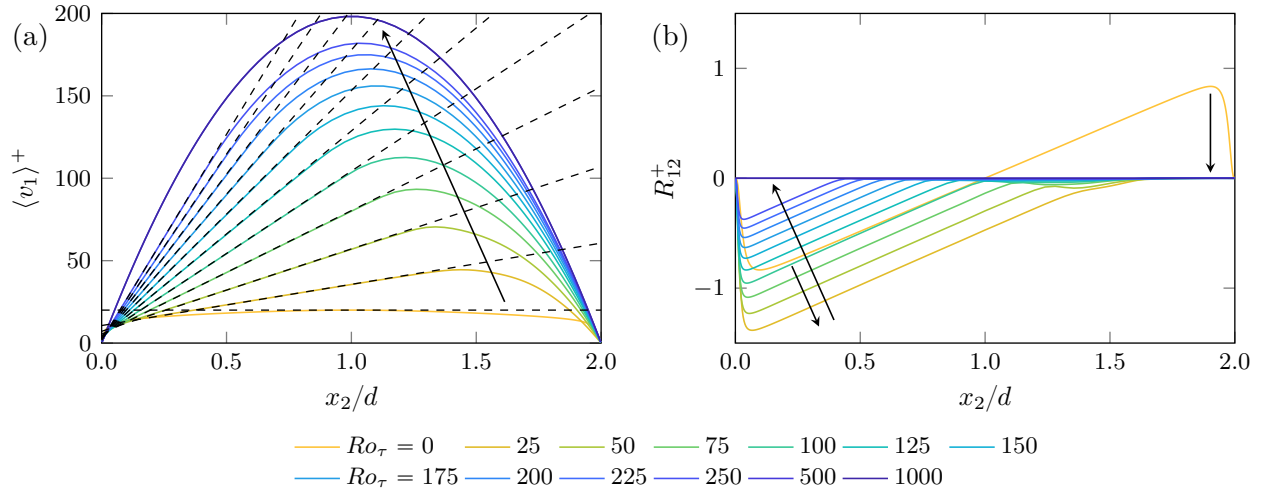


Figure 6: Rotation number dependence of the dimensionless (a) mean streamwise velocity and (b) Reynolds shear stress of spanwise-rotating plane-channel flow with friction Reynolds number $Re_\tau \approx 395$. Results were obtained from direct numerical simulations on a $256 \times 128 \times 256$ grid. The dashed lines have slope Ro_τ . Arrows indicate the direction of increasing rotation number.

the channel for the regions close to $x_2 = 0$ and $x_2 = 2d$, respectively.

Figure 7 shows the behavior of the diagonal Reynolds stresses of spanwise-rotating plane-channel flow. In the stable part of the channel, the streamwise Reynolds stress reduces as the rotation number increases, but not as quickly as the Reynolds shear stress (compare figures 7(a) and 6(b)). In the unstable part of the channel, the streamwise Reynolds stress reduces monotonically as the rotation number increases and seems to exhibit a linear behavior, as previously reported for $Re_\tau \approx 180$ by Xia et al. (2016). The wall-normal and spanwise Reynolds stresses, respectively provided in Fig. 7(b,c), quickly vanish in a growing (stable) region as the rotation number increases, but they exhibit a nonmonotonic behavior in the unstable part of the channel. Therefore, the turbulent kinetic energy, which is given by half the sum of the diagonal Reynolds stresses, does not vary monotonically with the rotation number, as previously observed for $Re_\tau \approx 180$ by Xia et al. (2016). In the unstable part of a spanwise-rotating channel, both the wall-normal and spanwise Reynolds stresses are larger than the streamwise stress, a feature that nonrotating channel flow does not have.

Although revealing important aspects of the behavior of spanwise-rotating plane-channel flow, the diagonal Reynolds stresses presented in Fig. 7 are not suitable as reference data for our LESs. Rather, since we employ traceless SGS models, we need to compare the (compensated) Reynolds stress anisotropy from our DNSs and LESs (Winckelmans et al. 2002). Figure 8 shows the diagonal elements of the Reynolds stress anisotropy computed from our DNSs. The most notable differences between the full and deviatoric Reynolds stresses of Figs. 7 and 8 are as follows. First, the streamwise Reynolds stress anisotropy, which is shown in Fig. 8(a), is (mostly) negative in the unstable part of rotating channel flow. Secondly, this quantity has the largest magnitude of all three normal stresses, although the wall-normal stress anisotropy shown in Fig. 8(b) is only slightly smaller. Finally, the spanwise Reynolds stress anisotropy, shown in Fig. 8(c), only attains a magnitude comparable to the other stresses close to the unstable wall, but otherwise is rather small. Since only the diagonal elements of the Reynolds stress anisotropy and Reynolds stress tensors differ, the Reynolds shear stress R_{12} of Fig. 6 remains as is. To summarize, spanwise-rotating plane-channel flow clearly exhibits a rich physical behavior with an interesting interplay between the Coriolis force and turbulence. As such, spanwise-rotating plane-channel flow forms a very interesting test case for LES.

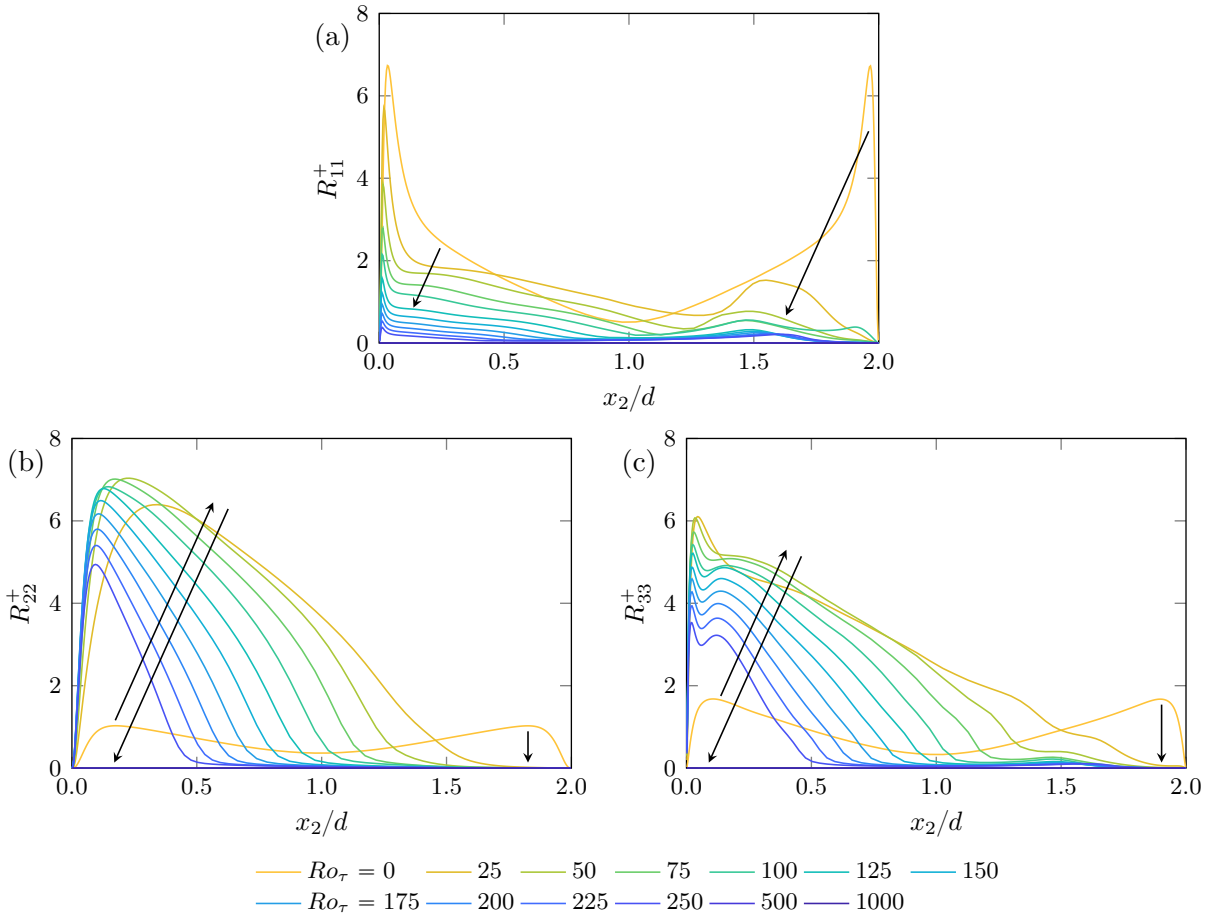


Figure 7: Rotation number dependence of the dimensionless (a) streamwise, (b) wall-normal and (c) spanwise Reynolds stress of spanwise-rotating plane-channel flow with friction Reynolds number $Re_\tau \approx 395$. Results were obtained from direct numerical simulations on a $256 \times 128 \times 256$ grid. Arrows indicate the direction of increasing rotation number.

5.2.3 LESs of spanwise-rotating plane-channel flow

In the current section, and in Sections 5.2.4 and 5.2.5, we present LESs of spanwise-rotating plane-channel flow. As in Section 5.1.4, these LESs were performed using the dynamic Smagorinsky model (Germano et al. 1991; Lilly 1992); the scaled anisotropic minimum-dissipation model (Verstappen 2018) with and without a supplemented nonlinear model term; two variants of the vortex-stretching-based eddy viscosity model (Silvis et al. 2017b; Silvis and Verstappen 2018); and the vortex-stretching-based nonlinear model of Eq. (26). We first discuss LESs of spanwise-rotating plane-channel flow with friction Reynolds number $Re_\tau \approx 395$ and rotation number $Ro_\tau = 100$ on a 32^3 grid. For $Ro_\tau = 100$, the interface between the stable laminar and unstable turbulent regions approximately lies in the middle of the channel. Given the stretching of the grid (refer to Eq. (41)), this rotation number can be expected to be most challenging for SGS models.

Table 3 shows the physical parameters as well as the grid spacings in units of the viscous length scales of our simulations. The LES without a model predicts a bulk Reynolds number that is too small and a friction Reynolds number corresponding to the unstable (stable) wall that is too high (low). The dynamic Smagorinsky model and the different vortex-stretching-based SGS models provide better predictions of these dimensionless numbers, whereas the scaled anisotropic minimum-dissipation model behaves worse than the no-model result. We will see corresponding behavior in predictions

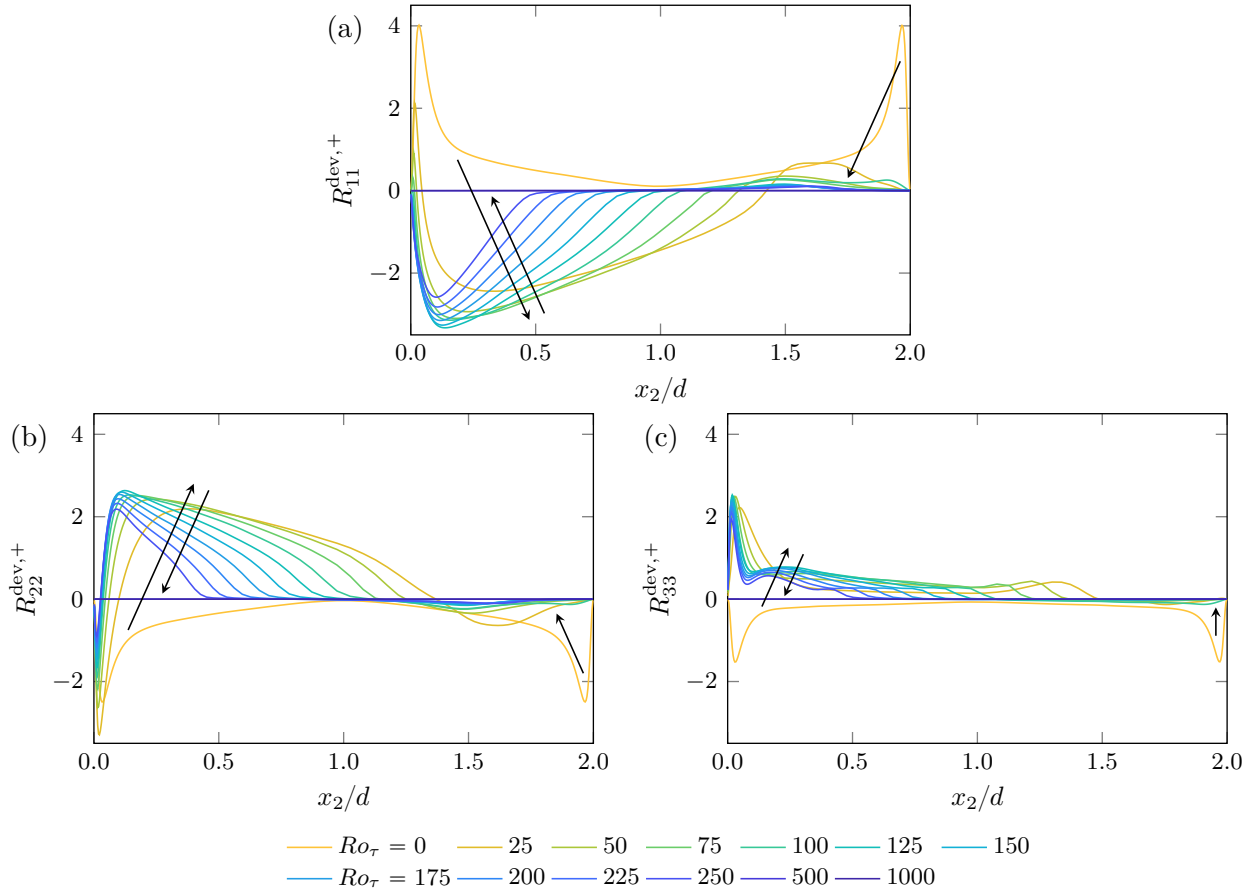


Figure 8: Rotation number dependence of the dimensionless (a) streamwise, (b) wall-normal and (c) spanwise Reynolds stress anisotropy of spanwise-rotating plane-channel flow with friction Reynolds number $Re_\tau \approx 395$. Results were obtained from direct numerical simulations on a $256 \times 128 \times 256$ grid. Arrows indicate the direction of increasing rotation number.

Table 3: Rotation and Reynolds numbers, and grid spacings in units of the viscous length scales of our numerical simulations of spanwise-rotating plane-channel flow with friction Reynolds number $Re_\tau \approx 395$ and friction rotation number $Ro_\tau = 100$. Details are shown of direct numerical simulations (DNSs) on a $256 \times 128 \times 256$ grid as well as of large-eddy simulations on a 32^3 grid without a model, and with the dynamic Smagorinsky model (DS); the scaled anisotropic minimum-dissipation model without (SAMD) and with a nonlinear model term with $C_\mu = 5$ (SAMD NL); the vortex-stretching-based eddy viscosity model with $C_\nu^2 \approx 0.34$ (VS EV1) and $C_\nu^2 \approx 0.17$ (VS EV2); and the vortex-stretching-based nonlinear model with $C_\nu^2 \approx 0.17$ and $C_\mu = 5$ (VS NL).

Label	Ro_b	Re_b	Re_τ	Re_τ^u	Re_τ^s	$\Delta x_1^{u,+}$	$\Delta x_1^{s,+}$	$\Delta x_2^{u,+}$	$\Delta x_2^{c,+}$	$\Delta x_2^{s,+}$	$\Delta x_3^{u,+}$	$\Delta x_3^{s,+}$
DNS	1.46	26 857	393	441	338	16	12	0.7	21	0.6	5	4
No model	1.62	24 400	395	454	325	134	96	3.0	78	2.2	45	32
DS	1.56	25 362	395	448	333	132	98	3.0	78	2.2	44	33
SAMD	1.63	24 270	395	437	348	129	103	2.9	78	2.3	43	34
SAMD NL	1.77	22 368	395	441	343	130	101	2.9	78	2.3	43	34
VS EV1	1.53	25 810	395	446	336	131	99	3.0	78	2.2	44	33
VS EV2	1.53	25 896	395	446	336	131	99	3.0	78	2.2	44	33
VS NL	1.58	25 035	395	449	332	132	98	3.0	78	2.2	44	33

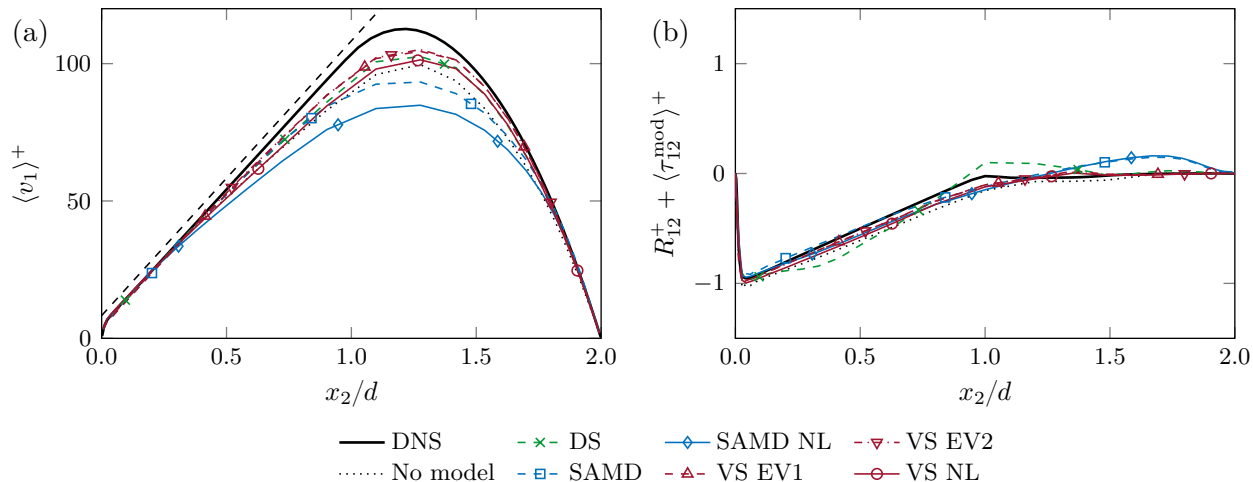


Figure 9: Predictions of the dimensionless (a) mean streamwise velocity and (b) compensated Reynolds shear stress of spanwise-rotating plane-channel flow with friction Reynolds number $Re_\tau \approx 395$ and friction rotation number $Ro_\tau = 100$. Results were obtained from direct numerical simulations (DNSs) on a $256 \times 128 \times 256$ grid as well as from large-eddy simulations (LESs) on a 32^3 grid without a model, and with the dynamic Smagorinsky model (DS); the scaled anisotropic minimum-dissipation model without (SAMD) and with a nonlinear model term with $C_\mu = 5$ (SAMD NL); the vortex-stretching-based eddy viscosity model with $C_\nu^2 \approx 0.34$ (VS EV1) and $C_\nu^2 \approx 0.17$ (VS EV2); and the vortex-stretching-based nonlinear model with $C_\nu^2 \approx 0.17$ and $C_\mu = 5$ (VS NL). The dashed line has slope $Ro_\tau = 100$.

of the mean streamwise velocity. The grid sizes in terms of the viscous length scales indicate that we consider coarse LESs (Georgiadis et al. 2010; Choi and Moin 2012). Specifically, the first grid point off the unstable wall is located at $\Delta x_2^{u,+} \approx 3.0$ in these simulations, which is larger than the recommended value $\Delta x_2^{u,+} \approx 1.0$.

Figure 9 shows predictions of the mean streamwise velocity and compensated Reynolds shear stress of spanwise-rotating plane-channel flow with friction Reynolds number $Re_\tau \approx 395$ and rotation number $Ro_\tau = 100$. Figure 9(a) shows that the dynamic Smagorinsky model and the vortex-stretching-based eddy viscosity models with $C_\nu^2 \approx 0.34$ and $C_\nu^2 \approx 0.17$ only slightly improve the prediction of the height and slope of the mean velocity with respect to the no-model result. The scaled anisotropic minimum-dissipation model provides a worse prediction than the simulation without a SGS model. The vortex-stretching-based nonlinear model (with $C_\nu^2 \approx 0.34$ and $C_\mu = 5$) predicts a mean streamwise velocity that lies very close to the result of the vortex-stretching-based eddy viscosity models. This is because predictions of the mean streamwise velocity are mostly determined by the eddy viscosity term and are not affected much by the nonlinear model term. Contrary to these observations, addition of the nonlinear model term to the scaled anisotropic minimum-dissipation model deteriorates the prediction of the mean velocity. Given the results of LESs on a 64^3 grid that we present in Section 5.2.5, this problem is likely caused by a lack of spatial resolution. Figure 9(b) shows that most SGS models predict a Reynolds shear stress that lies closer to the no-model result than to the reference data from DNSs. Predicting the mean streamwise velocity and Reynolds shear stress of spanwise-rotating plane-channel flow with $Re_\tau \approx 395$ and $Ro_\tau = 100$, thus, is very challenging for SGS models at a 32^3 grid resolution.

Figure 10 shows predictions of the diagonal elements of the compensated Reynolds stress anisotropy of spanwise-rotating plane-channel flow for $Ro_\tau = 100$ obtained on a 32^3 grid. The dynamic Smagorin-

LES (32^3), $Ro_\tau = 100$

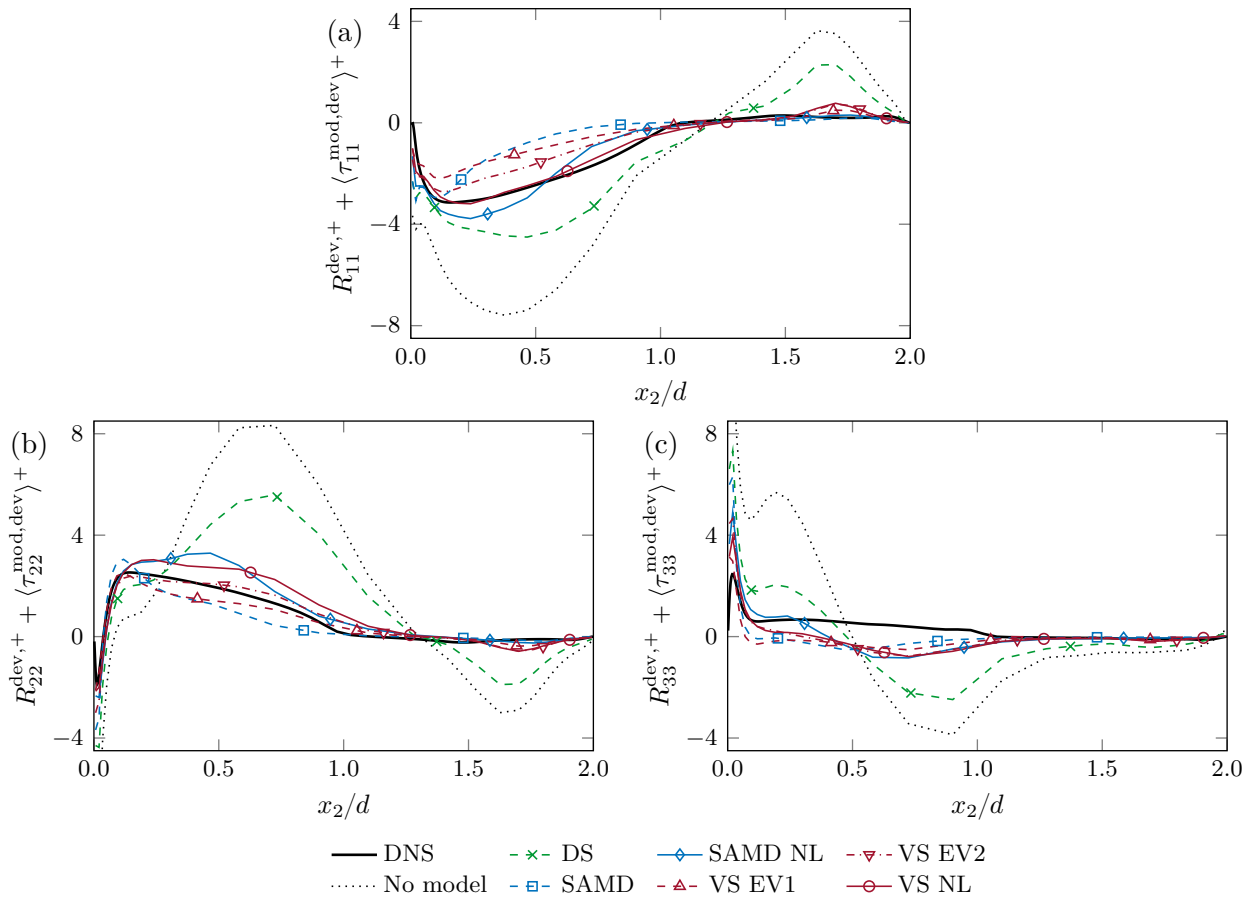


Figure 10: Predictions of the dimensionless compensated (a) streamwise, (b) wall-normal and (c) spanwise Reynolds stress anisotropy of spanwise-rotating plane-channel flow with friction Reynolds number $Re_\tau \approx 395$ and friction rotation number $Ro_\tau = 100$. Results were obtained from direct numerical simulations (DNSs) on a $256 \times 128 \times 256$ grid as well as from large-eddy simulations (LESs) on a 32^3 grid without a model, and with the dynamic Smagorinsky model (DS); the scaled anisotropic minimum-dissipation model without (SAMD) and with a nonlinear model term with $C_\mu = 5$ (SAMD NL); the vortex-stretching-based eddy viscosity model with $C_\nu^2 \approx 0.34$ (VS EV1) and $C_\nu^2 \approx 0.17$ (VS EV2); and the vortex-stretching-based nonlinear model with $C_\nu^2 \approx 0.17$ and $C_\mu = 5$ (VS NL).

sky model overpredicts the diagonal elements of the Reynolds stress anisotropy in both the unstable and stable parts of the channel. The results obtained using this model even qualitatively follow the no-model results. The scaled anisotropic minimum-dissipation model underpredicts the Reynolds stress anisotropy in most of the unstable part of the channel. Peaks close to the unstable wall do lie close to the reference data from DNSs, but tend to overshoot (see the wall-normal Reynolds stress anisotropy in Fig. 10(b)). The vortex-stretching-based eddy viscosity model with $C_\nu^2 \approx 0.34$ also underpredicts the Reynolds stress anisotropy in the unstable part of the channel. In addition, this model produces small peaks close to the unstable wall. The vortex-stretching-based eddy viscosity model with $C_\nu^2 \approx 0.17$ provides a good prediction of the wall-normal Reynolds stress anisotropy, but underpredicts the magnitude of the streamwise stress anisotropy. Eddy viscosity models, thus, fail to predict the Reynolds stress anisotropy of spanwise-rotating plane-channel flow at the current coarse resolution.

In contrast, the vortex-stretching-based nonlinear model provides an almost perfect prediction of

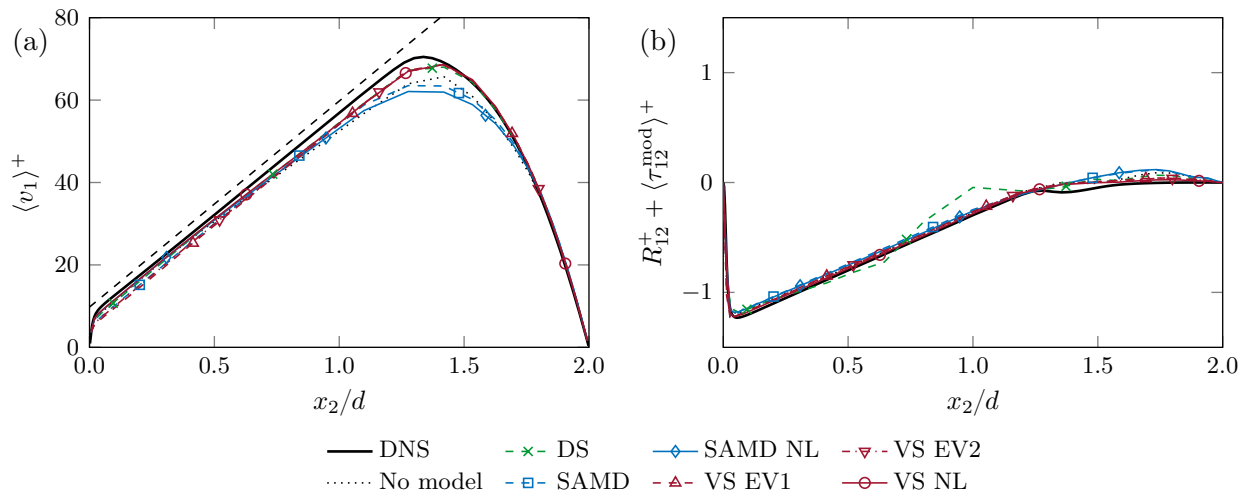


Figure 11: Predictions of the dimensionless (a) mean streamwise velocity and (b) compensated Reynolds shear stress of spanwise-rotating plane-channel flow with friction Reynolds number $Re_\tau \approx 395$ and friction rotation number $Ro_\tau = 50$. Results were obtained from direct numerical simulations (DNSs) on a $256 \times 128 \times 256$ grid as well as from large-eddy simulations (LESs) on a 32^3 grid without a model, and with the dynamic Smagorinsky model (DS); the scaled anisotropic minimum-dissipation model without (SAMD) and with a nonlinear model term with $C_\mu = 5$ (SAMD NL); the vortex-stretching-based eddy viscosity model with $C_\nu^2 \approx 0.34$ (VS EV1) and $C_\nu^2 \approx 0.17$ (VS EV2); and the vortex-stretching-based nonlinear model with $C_\nu^2 \approx 0.17$ and $C_\mu = 5$ (VS NL). The dashed line has slope $Ro_\tau = 50$.

the streamwise Reynolds stress anisotropy, as well as better predictions of the shape and magnitude of the wall-normal and spanwise Reynolds stress anisotropy than most considered eddy viscosity models. Specifically, the vortex-stretching-based nonlinear model does not produce any near-wall peaks in the Reynolds stress anisotropy. Although leading to a too high magnitude of the Reynolds stress anisotropy, addition of the nonlinear model term to the scaled anisotropic minimum-dissipation model also improves the shape of the predictions and removes the peaks near the unstable wall.

5.2.4 Rotation number dependence of LESs

We now generalize the observations of Section 5.2.3 to a large range of rotation rates. To that end, we first discuss Figs. 11 and 12, which show predictions of the mean streamwise velocity, compensated Reynolds shear stress and compensated Reynolds stress anisotropy of spanwise-rotating plane-channel flow with friction Reynolds number $Re_\tau \approx 395$ and rotation number $Ro_\tau = 50$ as obtained from LESs on a 32^3 grid.

Comparing Figs. 11 and 12 with Figs. 9 and 10, we see that all considered subgrid-scale models provide qualitatively similar predictions of spanwise-rotating plane-channel flow for $Ro_\tau = 50$ and $Ro_\tau = 100$, up to one notable difference. For $Ro_\tau = 50$, the scaled anisotropic minimum-dissipation model and the vortex-stretching-based eddy viscosity models with $C_\nu^2 \approx 0.34$ and $C_\nu^2 \approx 0.17$ produce large spurious peaks in the Reynolds stress anisotropy close to the unstable wall (see Fig. 12). These peaks likely arise due to a lack of dissipation of turbulent kinetic energy close to the unstable wall, which is caused by the coarse grid resolution in that area. The nonlinear model term entirely removes these near-wall peaks in the Reynolds stress anisotropy, as evidenced by the results of the vortex-stretching-based nonlinear model and the scaled anisotropic minimum-dissipation model with an

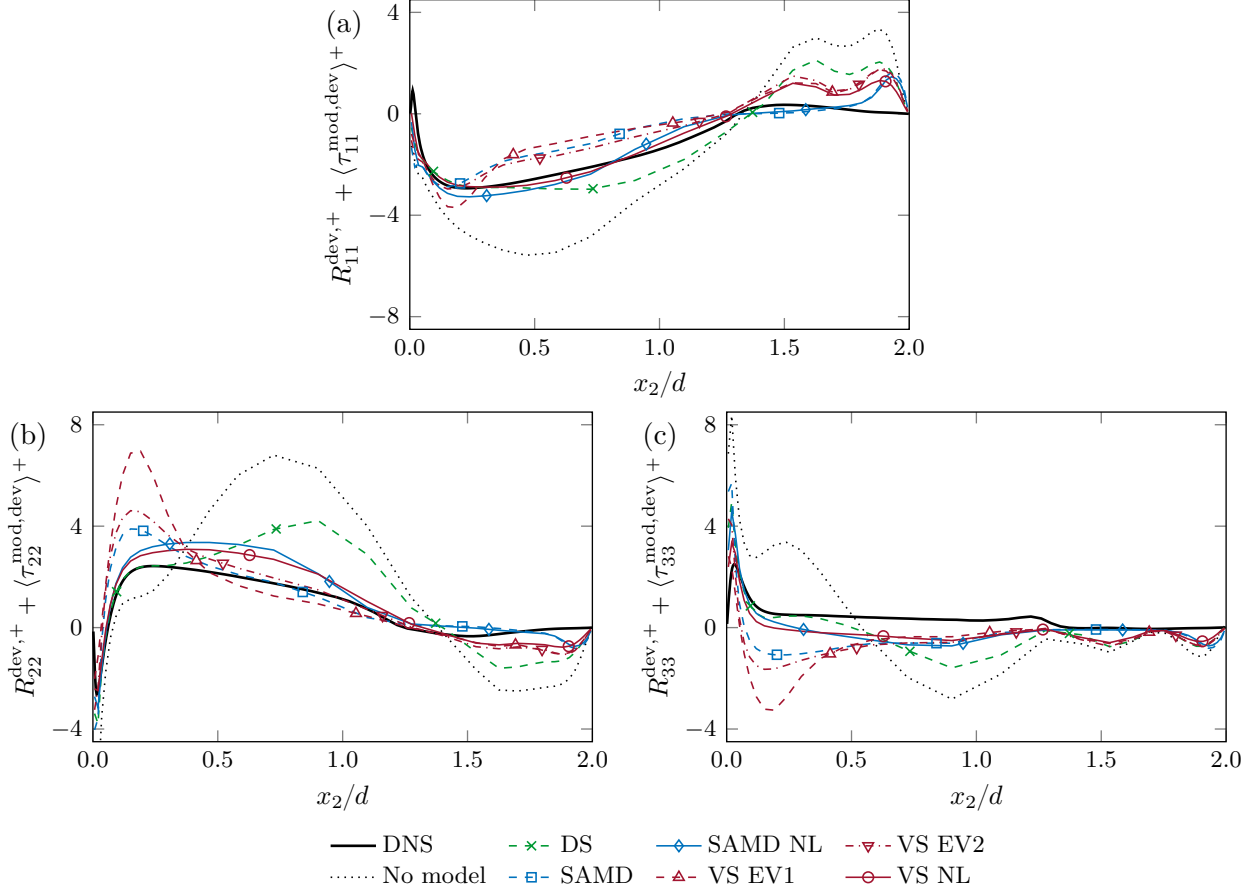


Figure 12: Predictions of the dimensionless compensated (a) streamwise, (b) wall-normal and (c) spanwise Reynolds stress anisotropy of spanwise-rotating plane-channel flow with friction Reynolds number $Re_\tau \approx 395$ and friction rotation number $Ro_\tau = 50$. Results were obtained from direct numerical simulations (DNSs) on a $256 \times 128 \times 256$ grid as well as from large-eddy simulations (LESs) on a 32^3 grid without a model, and with the dynamic Smagorinsky model (DS); the scaled anisotropic minimum-dissipation model without (SAMD) and with a nonlinear model term with $C_\mu = 5$ (SAMD NL); the vortex-stretching-based eddy viscosity model with $C_\nu^2 \approx 0.34$ (VS EV1) and $C_\nu^2 \approx 0.17$ (VS EV2); and the vortex-stretching-based nonlinear model with $C_\nu^2 \approx 0.17$ and $C_\mu = 5$ (VS NL).

added nonlinear term. The nonlinear model term of Eq. (26), thus, significantly improves predictions of the near-wall Reynolds stress anisotropy.

To further generalize the observations of Section 5.2.3, Fig. 13 shows the bulk Reynolds number and friction Reynolds numbers at both walls of spanwise-rotating plane-channel flow with $Re_\tau \approx 395$ and rotation numbers $Ro_\tau = 0 - 500$ as obtained from LESs on 32^3 grids. These bulk and friction Reynolds numbers respectively characterize the magnitude and shape of the mean velocity profile. For rotation numbers up to $Ro_\tau = 75$, the dynamic Smagorinsky and vortex-stretching-based SGS models predict bulk and friction Reynolds numbers that lie close to the reference results from our DNSs. For $100 \leq Ro_\tau \leq 250$, these models, however, predict a bulk Reynolds number that lies only slightly above the no-model result. These models also overpredict (underpredict) the friction Reynolds number at the unstable (stable) wall for this range of rotation numbers, but do improve the no-model result. The scaled anisotropic minimum-dissipation model greatly underpredicts the bulk Reynolds number and underpredicts (overpredicts) the friction Reynolds number at the unstable (stable) wall for most

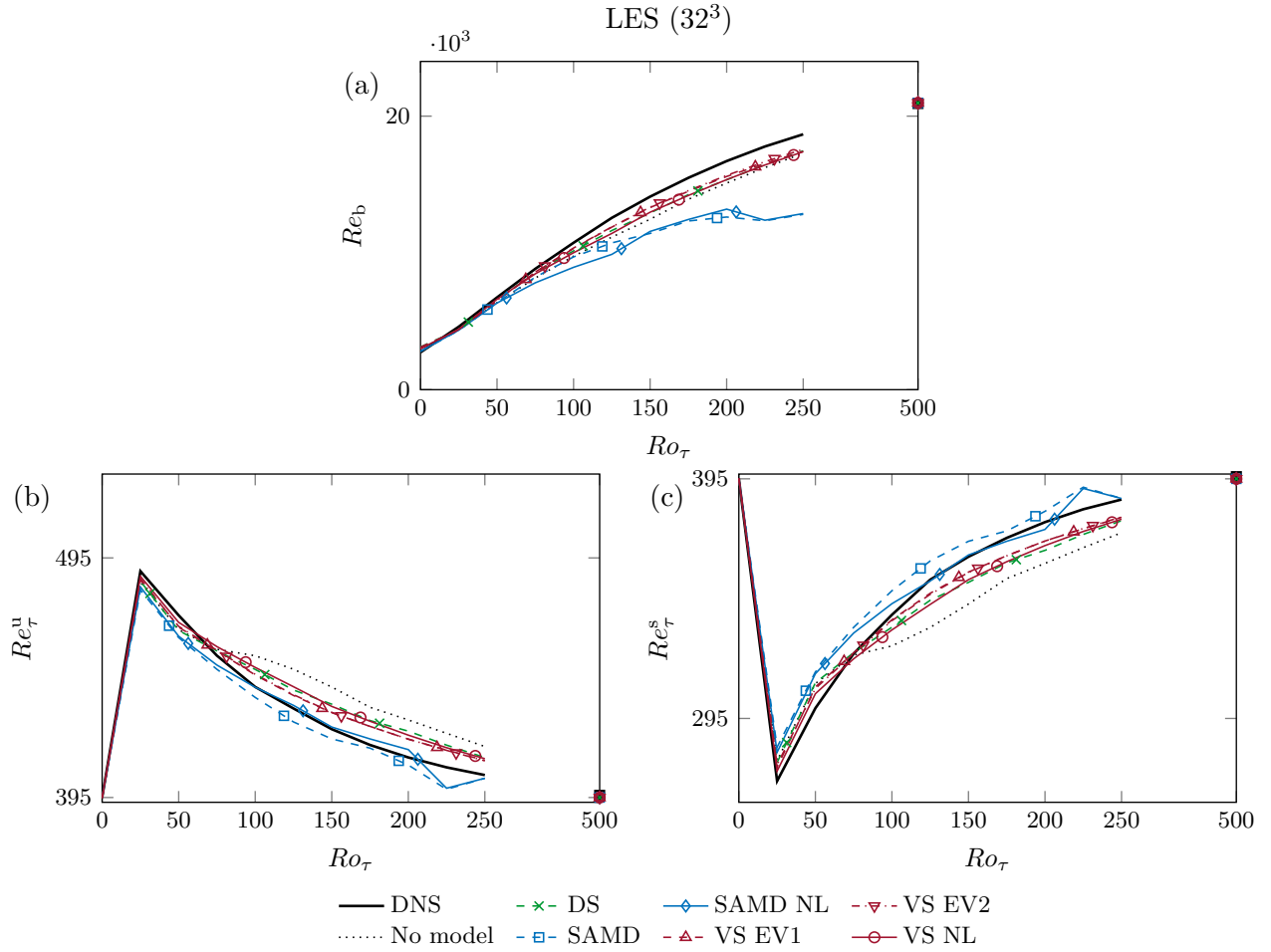


Figure 13: Rotation number dependence of predictions of the (a) bulk Reynolds number, (b) friction Reynolds number on the unstable side and (c) friction Reynolds number on the stable side of spanwise-rotating plane-channel flow with friction Reynolds number $Re_\tau \approx 395$. Results were obtained from direct numerical simulations (DNSs) on a $256 \times 128 \times 256$ grid as well as from large-eddy simulations (LESs) on a 32^3 grid without a model, and with the dynamic Smagorinsky model (DS); the scaled anisotropic minimum-dissipation model without (SAMD) and with a nonlinear model term with $C_\mu = 5$ (SAMD NL); the vortex-stretching-based eddy viscosity model with $C_\nu^2 \approx 0.34$ (VS EV1) and $C_\nu^2 \approx 0.17$ (VS EV2); and the vortex-stretching-based nonlinear model with $C_\nu^2 \approx 0.17$ and $C_\mu = 5$ (VS NL).

rotation numbers. All simulations (including the no-model LES) predict the correct bulk and friction Reynolds numbers of laminarized spanwise-rotating plane-channel flow at $Ro_\tau = 500$ and $Ro_\tau = 1000$, namely, $Re_b \approx 52312$ and $Re_\tau^u \approx Re_\tau^s \approx Re_\tau \approx 395$. The nonlinear model term has little effect on the bulk and friction Reynolds numbers. All considered SGS models, thus, provide predictions of the mean streamwise velocity that are qualitatively similar to the previously discussed cases with rotation numbers $Ro_\tau = 50$ and 100 for a large range of rotation rates. Specifically, the vortex-stretching-based SGS models provide predictions of the mean velocity that are as good as predictions obtained using the dynamic Smagorinsky model. The scaled anisotropic minimum-dissipation model usually (greatly) underpredicts the mean velocity and, thus, fails to predict this quantity. Furthermore, the mean velocity is mostly determined by the eddy viscosity and not affected much by the nonlinear model term.

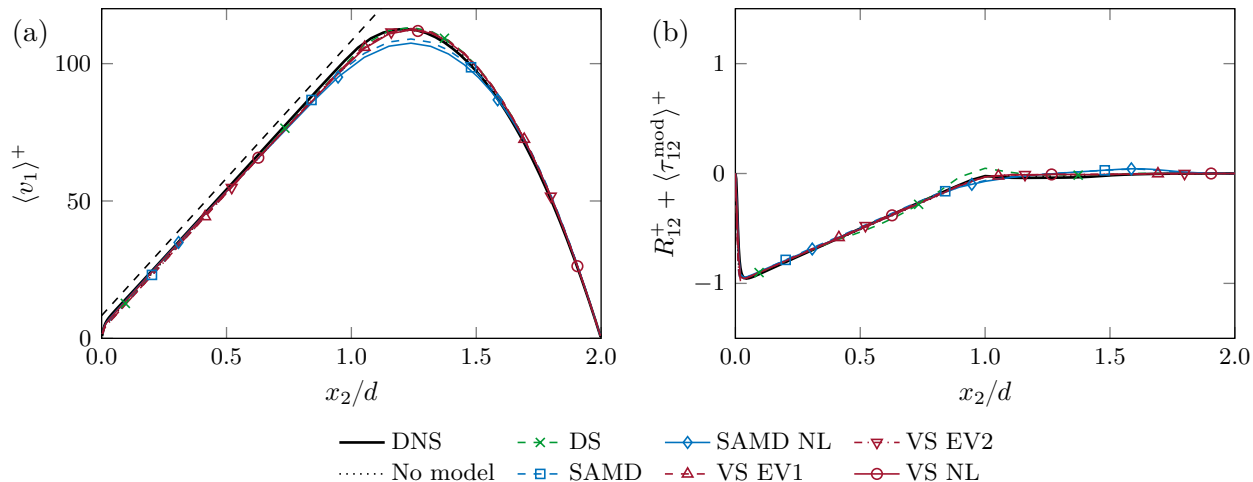


Figure 14: Predictions of the dimensionless (a) mean streamwise velocity and (b) compensated Reynolds shear stress of spanwise-rotating plane-channel flow with friction Reynolds number $Re_\tau \approx 395$ and friction rotation number $Ro_\tau = 100$. Results were obtained from direct numerical simulations (DNSs) on a $256 \times 128 \times 256$ grid as well as from large-eddy simulations (LESs) on a 64^3 grid without a model, and with the dynamic Smagorinsky model (DS); the scaled anisotropic minimum-dissipation model without (SAMD) and with a nonlinear model term with $C_\mu = 5$ (SAMD NL); the vortex-stretching-based eddy viscosity model with $C_\nu^2 \approx 0.34$ (VS EV1) and $C_\nu^2 \approx 0.17$ (VS EV2); and the vortex-stretching-based nonlinear model with $C_\nu^2 \approx 0.17$ and $C_\mu = 5$ (VS NL). The dashed line has slope $Ro_\tau = 100$.

On the other hand, predictions of the Reynolds stress anisotropy are affected, and improved significantly, by the nonlinear model term over a large range of rotation numbers. We have observed that the vortex-stretching-based nonlinear model provides much better predictions of the Reynolds stress anisotropy than the considered eddy viscosity models for the rotation numbers from $Ro_\tau = 50$ to $Ro_\tau = 250$ (as shown for $Ro_\tau = 50$ and $Ro_\tau = 100$ in Figs. 10 and 12). The nonlinear term of the vortex-stretching-based nonlinear model plays a key role in this by improving predictions of the near-wall Reynolds stress anisotropy. Over this range of rotation rates, the same model constants as in Sections 5.1.4 and 5.2.3 can be used without requiring (dynamic) adaptation or near-wall damping. For $Ro_\tau = 25$, the vortex-stretching-based nonlinear model term also leads to improved predictions of the Reynolds stress anisotropy when compared to eddy viscosity models. In this case, taking $C_\nu^2 \approx 0.34$ rather than $C_\nu^2 \approx 0.17$ may be beneficial, however. In a flow without spanwise rotation, for which $Ro_\tau = 0$, the nonlinear term of the vortex-stretching-based nonlinear model has almost no effect on predictions of the Reynolds stress anisotropy. These predictions are, then, determined by the eddy viscosity term. For the very high rotation rates for which full laminarization occurs, such as $Ro_\tau = 500$ and 1000, the nonlinear model properly turns off.

5.2.5 Resolution dependence of LESs

To determine the effects of the grid resolution on our LES results, Figs. 14 and 15 show predictions of the mean streamwise velocity, compensated Reynolds shear stress and compensated diagonal elements of the Reynolds stress anisotropy of spanwise-rotating plane-channel flow with friction Reynolds number $Re_\tau \approx 395$ and rotation number $Ro_\tau = 100$ as obtained from LESs on a 64^3 grid. All considered SGS models give a very good prediction of the mean streamwise velocity and Reynolds

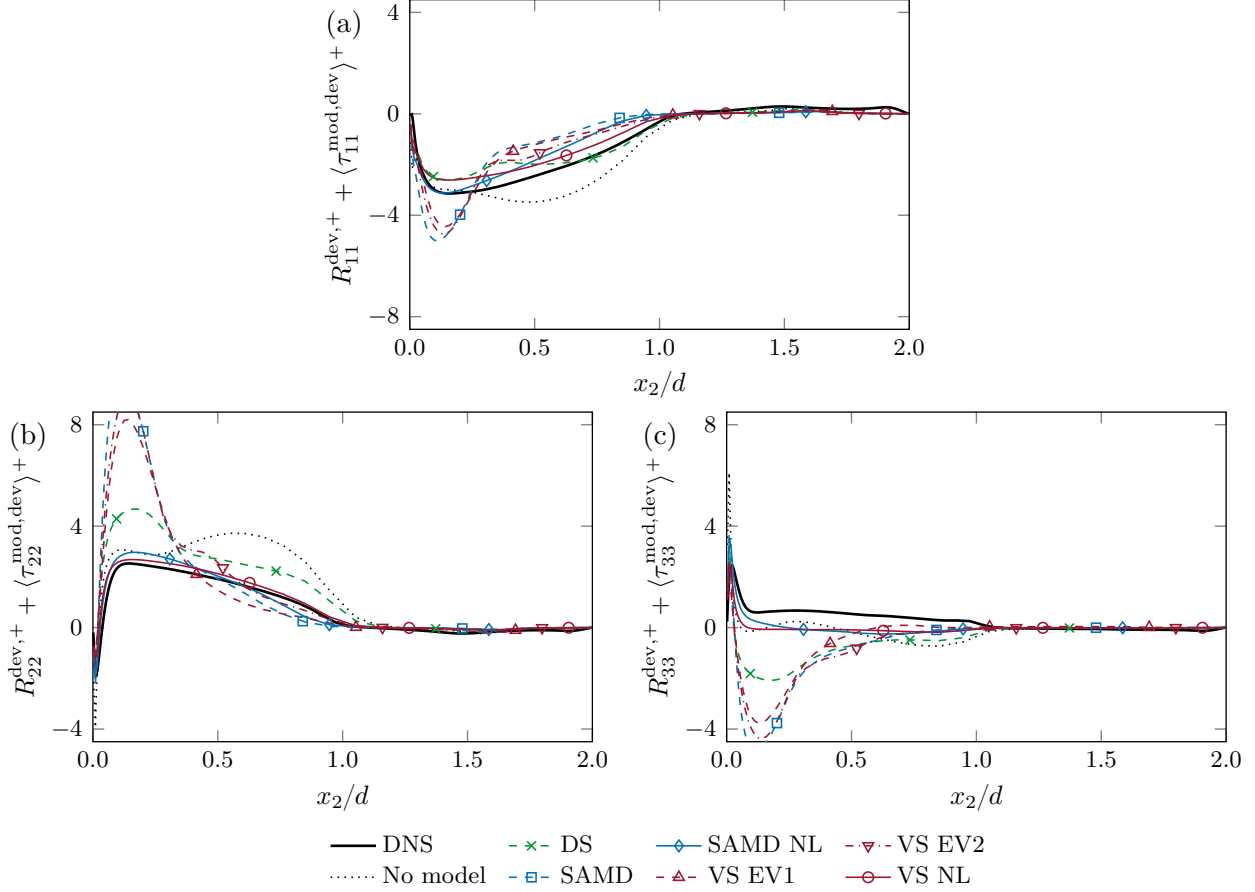


Figure 15: Predictions of the dimensionless compensated (a) streamwise, (b) wall-normal and (c) spanwise Reynolds stress anisotropy of spanwise-rotating plane-channel flow with friction Reynolds number $Re_\tau \approx 395$ and friction rotation number $Ro_\tau = 100$. Results were obtained from direct numerical simulations (DNSs) on a $256 \times 128 \times 256$ grid as well as from large-eddy simulations (LESs) on a 64^3 grid without a model, and with the dynamic Smagorinsky model (DS); the scaled anisotropic minimum-dissipation model without (SAMD) and with a nonlinear model term with $C_\mu = 5$ (SAMD NL); the vortex-stretching-based eddy viscosity model with $C_\nu^2 \approx 0.34$ (VS EV1) and $C_\nu^2 \approx 0.17$ (VS EV2); and the vortex-stretching-based nonlinear model with $C_\nu^2 \approx 0.17$ and $C_\mu = 5$ (VS NL).

shear stress for this resolution and rotation number (refer to Fig. 14(a)). Good predictions of these quantities are also provided over the range of rotation numbers $50 \leq Ro_\tau \leq 200$ by all SGS models but the scaled anisotropic minimum-dissipation model.

The predictions of the Reynolds stress anisotropy obtained using the dynamic Smagorinsky model improved significantly with respect to the results obtained on a 32^3 grid (compare Fig. 10). Nonetheless, the dynamic Smagorinsky model produces spurious peaks in the Reynolds stress anisotropy close to the unstable wall. Similarly, the vortex-stretching-based eddy viscosity models with $C_\nu^2 \approx 0.34$ and $C_\nu^2 \approx 0.17$ predict very large spurious peaks close to the unstable wall. Since we implemented these latter models using Deardorff's length scale (see Eq. (30)), it seems likely that these peaks are caused by a lack of near-wall dissipation by the SGS model (Trias et al. 2017). Also the scaled anisotropic minimum-dissipation model causes spurious near-wall peaks in the Reynolds stress anisotropy. We obtained similar predictions over the range of rotation numbers from $Ro_\tau = 75$ to 200. The considered eddy viscosity models, thus, fail to give good predictions of the Reynolds stress anisotropy on both

32^3 and 64^3 grid.

As was the case for the LESs of spanwise-rotating plane-channel flow with $Ro_\tau = 50$ on a 32^3 grid, the spurious near-wall peaks produced by the scaled anisotropic minimum-dissipation model and the vortex-stretching-based eddy viscosity model with $C_\nu^2 \approx 0.17$ are removed entirely by adding the nonlinear term. Moreover, with this improved description of near-wall effects, these nonlinear models both give very good predictions of the Reynolds stress anisotropy. Again qualitatively similar predictions were obtained for $75 \leq Ro_\tau \leq 200$. The vortex-stretching-based nonlinear model, thus, gives outstanding predictions of spanwise-rotating plane-channel flow in LESs with both fine (64^3) and coarse (32^3) spatial resolutions, and outperforms the dynamic Smagorinsky and scaled anisotropic minimum-dissipation models without requiring (near-wall) damping or dynamic adaptation of the model constants.

6 Conclusions and outlook

In this work, we aimed to improve the numerical prediction of incompressible rotating turbulent flows. To that end, we proposed and validated a new nonlinear SGS model for LESs of such flows.

In particular, we first discussed the need for SGS modeling of rotating flows. Using a general class of SGS models that can parametrize both dissipative and nondissipative processes, we then proposed a new SGS model for LESs of rotating turbulent flows. The first term of this SGS model is a dissipative eddy viscosity term that is linear in the rate-of-strain tensor, while the second term, which is nonlinear in the rate-of-strain and rate-of-rotation tensors, is nondissipative. We defined the two corresponding model coefficients in terms of the vortex stretching magnitude and named the resulting model the vortex-stretching-based nonlinear model. The vortex-stretching-based nonlinear model by construction is consistent with many physical and mathematical properties of the Navier–Stokes equations and turbulent stresses. This model, therefore, respects fundamental properties of turbulent flows and can be used in complex flow configurations without requiring near-wall damping functions or dynamic procedures. Being based on the local velocity gradient and grid size, the vortex-stretching-based nonlinear model also is easy to implement. To preserve the different nature of the two terms of the model in numerical simulations, we recommended a purely dissipative implementation for the eddy viscosity term, whereas the nonlinear term should conserve kinetic energy. We also recommended the use of a discretization in which the convective and Coriolis force terms of the incompressible Navier–Stokes equations conserve kinetic energy, and in which the diffusive only causes dissipation.

We studied and validated the vortex-stretching-based nonlinear model using detailed DNSs and LESs of rotating decaying turbulence and spanwise-rotating plane-channel flow. We also compared the predictions from this model with predictions from the commonly used dynamic Smagorinsky model, the scaled anisotropic minimum-dissipation model and the vortex-stretching-based eddy viscosity model.

Using LESs of rotating decaying turbulence, we revealed that the two terms of the vortex-stretching-based nonlinear model describe distinct physical effects. The eddy viscosity and nonlinear terms, respectively, cause dissipation and transfer of energy. We also showed that the two terms interact with each other. The commonly used assumption that dissipative eddy viscosity and nondissipative nonlinear terms can be treated separately, thus, is invalid. We, therefore, proposed a nondynamic procedure to determine the model constants of the vortex-stretching-based nonlinear model, which takes into account the interplay between the two model terms. For the resulting model constants, the eddy viscosity term models dissipation of energy, while the nonlinear term accounts for backscatter of energy. As such the vortex-stretching-based nonlinear model provided good predictions of nonrotating and rotating decaying turbulence, performing as well as the dynamic Smagorinsky and scaled anisotropic minimum-dissipation models.

We subsequently showed that the dynamic Smagorinsky model, the scaled anisotropic minimum-

dissipation model and the vortex-stretching-based eddy viscosity model fail to predict the Reynolds stress anisotropy of spanwise-rotating plane-channel flow. These eddy viscosity models specifically tend to produce spurious near-wall peaks in predictions of the Reynolds stress anisotropy. On coarse grids, the scaled anisotropic minimum-dissipation model even failed to predict the mean streamwise velocity. Spanwise-rotating plane-channel flow, thus, forms a challenging test case for eddy viscosity models. In contrast, the vortex-stretching-based nonlinear model gave outstanding predictions of spanwise-rotating plane-channel flow over a large range of rotation rates, for both fine and coarse grid resolutions. The nonlinear model term played a key role in this, by improving predictions of the near-wall Reynolds stress anisotropy. The same model constants that were determined using LESs of rotating decaying turbulence could be used for the LESs of spanwise-rotating plane-channel flow. The vortex-stretching-based nonlinear model, thus, performs as well as the dynamic Smagorinsky and scaled anisotropic minimum-dissipation models in LESs of rotating decaying turbulence and outperforms these models in LESs of spanwise-rotating plane-channel flow, without requiring (dynamic) adaptation or near-wall damping of the model constants.

In future work, it would be interesting to investigate in detail the performance of the vortex-stretching-based nonlinear model in LESs of (different) rotating turbulent flows with a higher Reynolds number. One could also analyze the ability of the vortex-stretching-based nonlinear model to predict (coherent) flow structures, such as the Taylor–Görtler vortices that occur in spanwise-rotating plane-channel flow (Dai et al. 2016). Other points of interest for future studies could be adaptation of the vortex-stretching-based nonlinear model to simulate rotating turbulent flows from an inertial frame of reference, or adaptation of the subgrid characteristic length scale (see, e.g., Trias et al. 2017). Finally, our results indicate that supplementing the scaled anisotropic minimum-dissipation model with the nonlinear term of the vortex-stretching-based nonlinear model is beneficial. Combining this nonlinear term with other eddy viscosity models could also be interesting, as long as the interplay between the eddy viscosity and nonlinear terms is taken into account.

Acknowledgments The authors gratefully acknowledge Geert Brethouwer for his support in identifying turbulent bursts in spanwise-rotating plane-channel flow. M.H.S. is supported by the research programme Free Competition in the Physical Sciences (Project No. 613.001.212), which is financed by the Netherlands Organization for Scientific Research (NWO). F.X.T. is supported by a Ramón y Cajal postdoctoral contract (No. RYC-2012-11996) financed by the Ministerio de Economía y Competitividad, Spain. Part of this research was conducted during the Center for Turbulence Research (CTR) Summer Program 2016 at Stanford University. M.H.S., F.X.T. and R.V. thank the CTR for its hospitality and financial support. We would like to thank the Center for Information Technology of the University of Groningen for their support and for providing access to the Peregrine high-performance computing cluster. The authors also acknowledge use of computational resources from the Certainty cluster awarded by the National Science Foundation to CTR and from the MareNostrum supercomputer at the Barcelona Supercomputing Center.

References

- Alexakis, A. and Biferale, L. (2018). “Cascades and transitions in turbulent flows”. In: *Phys. Rep.* 767–769, pp. 1–101. DOI: [10.1016/j.physrep.2018.08.001](https://doi.org/10.1016/j.physrep.2018.08.001).
- Bardina, J., Ferziger, J. H., and Reynolds, W. C. (1983). *Improved turbulence models based on large eddy simulation of homogeneous, incompressible, turbulent flows*. Technical Report TF-19. Stanford University.
- Bardina, J., Ferziger, J. H., and Rogallo, R. S. (1985). “Effect of rotation on isotropic turbulence: computation and modelling”. In: *J. Fluid Mech.* 154, pp. 321–336. DOI: [10.1017/S0022112085001550](https://doi.org/10.1017/S0022112085001550).

- Bourouiba, L. and Bartello, P. (2007). “The intermediate Rossby number range and two-dimensional–three-dimensional transfers in rotating decaying homogeneous turbulence”. In: *J. Fluid Mech.* 587, pp. 139–161. DOI: [10.1017/S0022112007007124](https://doi.org/10.1017/S0022112007007124).
- Bourouiba, L., Straub, D. N., and Waite, M. L. (2012). “Non-local energy transfers in rotating turbulence at intermediate Rossby number”. In: *J. Fluid Mech.* 690, pp. 129–147. DOI: [10.1017/jfm.2011.387](https://doi.org/10.1017/jfm.2011.387).
- Brethouwer, G. (2016). “Linear instabilities and recurring bursts of turbulence in rotating channel flow simulations”. In: *Phys. Rev. Fluids* 1, 054404. DOI: [10.1103/PhysRevFluids.1.054404](https://doi.org/10.1103/PhysRevFluids.1.054404).
- Brethouwer, G. (2017). “Statistics and structure of spanwise rotating turbulent channel flow at moderate Reynolds numbers”. In: *J. Fluid Mech.* 828, pp. 424–458. DOI: [10.1017/jfm.2017.526](https://doi.org/10.1017/jfm.2017.526).
- Brethouwer, G., Schlatter, P., Duguet, Y., Henningson, D. S., and Johansson, A. V. (2014). “Recurrent Bursts via Linear Processes in Turbulent Environments”. In: *Phys. Rev. Lett.* 112, 144502. DOI: [10.1103/PhysRevLett.112.144502](https://doi.org/10.1103/PhysRevLett.112.144502).
- Buzzicotti, M., Aluie, H., Biferale, L., and Linkmann, M. (2018). “Energy transfer in turbulence under rotation”. In: *Phys. Rev. Fluids* 3, 034802. DOI: [10.1103/PhysRevFluids.3.034802](https://doi.org/10.1103/PhysRevFluids.3.034802).
- Cambon, C., Mansour, N. N., and Godeferd, F. S. (1997). “Energy transfer in rotating turbulence”. In: *J. Fluid Mech.* 337, pp. 303–332. DOI: [10.1017/S002211209700493X](https://doi.org/10.1017/S002211209700493X).
- Carati, D., Winckelmans, G. S., and Jeanmart, H. (2001). “On the modelling of the subgrid-scale and filtered-scale stress tensors in large-eddy simulation”. In: *J. Fluid Mech.* 441, pp. 119–138. DOI: [10.1017/S0022112001004773](https://doi.org/10.1017/S0022112001004773).
- Chapman, D. R. and Kuhn, G. D. (1986). “The limiting behaviour of turbulence near a wall”. In: *J. Fluid Mech.* 170, pp. 265–292. DOI: [10.1017/S0022112086000885](https://doi.org/10.1017/S0022112086000885).
- Chen, Q., Chen, S., Eyink, G. L., and Holm, D. D. (2005). “Resonant interactions in rotating homogeneous three-dimensional turbulence”. In: *J. Fluid Mech.* 542, pp. 139–164. DOI: [10.1017/S0022112005006324](https://doi.org/10.1017/S0022112005006324).
- Cheviakov, A. F. and Oberlack, M. (2014). “Generalized Ertel’s theorem and infinite hierarchies of conserved quantities for three-dimensional time-dependent Euler and Navier–Stokes equations”. In: *J. Fluid Mech.* 760, pp. 368–386. DOI: [10.1017/jfm.2014.611](https://doi.org/10.1017/jfm.2014.611).
- Choi, H. and Moin, P. (2012). “Grid-point requirements for large eddy simulation: Chapman’s estimates revisited”. In: *Phys. Fluids* 24, 011702. DOI: [10.1063/1.3676783](https://doi.org/10.1063/1.3676783).
- Clark, R. A., Ferziger, J. H., and Reynolds, W. C. (1979). “Evaluation of subgrid-scale models using an accurately simulated turbulent flow”. In: *J. Fluid Mech.* 91, pp. 1–16. DOI: [10.1017/S002211207900001X](https://doi.org/10.1017/S002211207900001X).
- Comte-Bellot, G. and Corrsin, S. (1971). “Simple Eulerian time correlation of full- and narrow-band velocity signals in grid-generated, ‘isotropic’ turbulence”. In: *J. Fluid Mech.* 48, pp. 273–337. DOI: [10.1017/S0022112071001599](https://doi.org/10.1017/S0022112071001599).
- Dai, Y.-J., Huang, W.-X., and Xu, C.-X. (2016). “Effects of Taylor–Görtler vortices on turbulent flows in a spanwise-rotating channel”. In: *Phys. Fluids* 28, 115104. DOI: [10.1063/1.4967702](https://doi.org/10.1063/1.4967702).
- Deardorff, J. W. (1970). “Numerical study of three-dimensional turbulent channel flow at large Reynolds numbers”. In: *J. Fluid Mech.* 41, pp. 453–480. DOI: [10.1017/S0022112070000691](https://doi.org/10.1017/S0022112070000691).
- Georgiadis, N. J., Rizzetta, D. P., and Fureby, C. (2010). “Large-Eddy Simulation: Current Capabilities, Recommended Practices, and Future Research”. In: *AIAA J.* 48, pp. 1772–1784. DOI: [10.2514/1.J050232](https://doi.org/10.2514/1.J050232).
- Germano, M., Piomelli, U., Moin, P., and Cabot, W. H. (1991). “A dynamic subgrid-scale eddy viscosity model”. In: *Phys. Fluids A* 3, pp. 1760–1765. DOI: [10.1063/1.857955](https://doi.org/10.1063/1.857955).
- Godeferd, F. S. and Moisy, F. (2015). “Structure and Dynamics of Rotating Turbulence: A Review of Recent Experimental and Numerical Results”. In: *Appl. Mech. Rev.* 67, 030802. DOI: [10.1115/1.4029006](https://doi.org/10.1115/1.4029006).
- Grundestam, O., Wallin, S., and Johansson, A. V. (2008). “Direct numerical simulations of rotating turbulent channel flow”. In: *J. Fluid Mech.* 598, pp. 177–199. DOI: [10.1017/S0022112007000122](https://doi.org/10.1017/S0022112007000122).

- Hopfinger, E. J., Browand, F. K., and Gagne, Y. (1982). “Turbulence and waves in a rotating tank”. In: *J. Fluid Mech.* 125, pp. 505–534. DOI: [10.1017/S0022112082003462](https://doi.org/10.1017/S0022112082003462).
- Horiuti, K. (2003). “Roles of non-aligned eigenvectors of strain-rate and subgrid-scale stress tensors in turbulence generation”. In: *J. Fluid Mech.* 491, pp. 65–100. DOI: [10.1017/S0022112003005299](https://doi.org/10.1017/S0022112003005299).
- Huang, X., Liu, Z., Yang, W., Li, Y., and Yang, Z. (2017). “A Cubic Nonlinear Subgrid-Scale Model for Large Eddy Simulation”. In: *J. Fluid. Eng. - T. ASME* 139, 041101. DOI: [10.1115/1.4035217](https://doi.org/10.1115/1.4035217).
- Jacquin, L., Leuchter, O., Cambon, C., and Mathieu, J. (1990). “Homogeneous turbulence in the presence of rotation”. In: *J. Fluid Mech.* 220, pp. 1–52. DOI: [10.1017/S0022112090003172](https://doi.org/10.1017/S0022112090003172).
- Johnston, J. P., Halleen, R. M., and Lezius, D. K. (1972). “Effects of spanwise rotation on the structure of two-dimensional fully developed turbulent channel flow”. In: *J. Fluid Mech.* 56, pp. 533–557. DOI: [10.1017/S0022112072002502](https://doi.org/10.1017/S0022112072002502).
- Kang, H. S., Chester, S., and Meneveau, C. (2003). “Decaying turbulence in an active-grid-generated flow and comparisons with large-eddy simulation”. In: *J. Fluid Mech.* 480, pp. 129–160. DOI: [10.1017/S0022112002003579](https://doi.org/10.1017/S0022112002003579).
- Kim, J. and Moin, P. (1985). “Application of a fractional-step method to incompressible Navier–Stokes equations”. In: *J. Comput. Phys.* 59, pp. 308–323. DOI: [10.1016/0021-9991\(85\)90148-2](https://doi.org/10.1016/0021-9991(85)90148-2).
- Kosović, B. (1997). “Subgrid-scale modelling for the large-eddy simulation of high-Reynolds-number boundary layers”. In: *J. Fluid Mech.* 336, pp. 151–182. DOI: [10.1017/S0022112096004697](https://doi.org/10.1017/S0022112096004697).
- Kristoffersen, R. and Andersson, H. I. (1993). “Direct simulations of low-Reynolds-number turbulent flow in a rotating channel”. In: *J. Fluid Mech.* 256, pp. 163–197. DOI: [10.1017/S0022112093002757](https://doi.org/10.1017/S0022112093002757).
- Kwak, D., Reynolds, W. C., and Ferziger, J. H. (1975). *Three-Dimensional, Time Dependent Computation of Turbulent Flow*. Technical Report TF-5. Stanford University.
- Lamballais, E., Lesieur, M., and Métais, O. (1996). “Effects of spanwise rotation on the vorticity stretching in transitional and turbulent channel flow”. In: *Int. J. Heat Fluid Fl.* 17, pp. 324–332. DOI: [10.1016/0142-727X\(96\)00043-4](https://doi.org/10.1016/0142-727X(96)00043-4).
- Leonard, A. (1975). “Energy Cascade in Large-Eddy Simulations of Turbulent Fluid Flows”. In: *Turbulent Diffusion in Environmental Pollution. Proceedings of a Symposium held at Charlottesville, Virginia, April 8-14, 1973*. Ed. by Frenkiel, F. N. and Munn, R. E. Vol. 18 A. Adv. Geophys. Elsevier, pp. 237–248. DOI: [10.1016/S0065-2687\(08\)60464-1](https://doi.org/10.1016/S0065-2687(08)60464-1).
- Lilly, D. K. (1992). “A proposed modification of the Germano subgrid-scale closure method”. In: *Phys. Fluids A* 4, pp. 633–635. DOI: [10.1063/1.858280](https://doi.org/10.1063/1.858280).
- Liu, N., Lu, X., and Zhuang, L. (2004). “An improved dynamic subgrid-scale model and its application to large eddy simulation of rotating channel flows”. In: *Sci. China Ser. G* 47, pp. 463–476. DOI: [10.1360/03yw0228](https://doi.org/10.1360/03yw0228).
- Liu, S., Meneveau, C., and Katz, J. (1994). “On the properties of similarity subgrid-scale models as deduced from measurements in a turbulent jet”. In: *J. Fluid Mech.* 275, pp. 83–119. DOI: [10.1017/S0022112094002296](https://doi.org/10.1017/S0022112094002296).
- Lund, T. S. and Novikov, E. A. (1992). “Parameterization of subgrid-scale stress by the velocity gradient tensor”. In: *Annual Research Briefs*, Center for Turbulence Research, Stanford University, pp. 27–43.
- Marstorp, L., Brethouwer, G., Grundestam, O., and Johansson, A. V. (2009). “Explicit algebraic subgrid stress models with application to rotating channel flow”. In: *J. Fluid Mech.* 639, pp. 403–432. DOI: [10.1017/S0022112009991054](https://doi.org/10.1017/S0022112009991054).
- Mininni, P. D., Alexakis, A., and Pouquet, A. (2009). “Scale interactions and scaling laws in rotating flows at moderate Rossby numbers and large Reynolds numbers”. In: *Phys. Fluids* 21, 015108. DOI: [10.1063/1.3064122](https://doi.org/10.1063/1.3064122).
- Montecchia, M., Brethouwer, G., Johansson, A. V., and Wallin, S. (2017). “Taking large-eddy simulation of wall-bounded flows to higher Reynolds numbers by use of anisotropy-resolving subgrid models”. In: *Phys. Rev. Fluids* 2, 034601. DOI: [10.1103/PhysRevFluids.2.034601](https://doi.org/10.1103/PhysRevFluids.2.034601).

- Morize, C., Moisy, F., and Rabaud, M. (2005). “Decaying grid-generated turbulence in a rotating tank”. In: *Phys. Fluids* 17, 095105. DOI: [10.1063/1.2046710](https://doi.org/10.1063/1.2046710).
- Nakabayashi, K. and Kitoh, O. (2005). “Turbulence characteristics of two-dimensional channel flow with system rotation”. In: *J. Fluid Mech.* 528, pp. 355–377. DOI: [10.1017/S0022112004002939](https://doi.org/10.1017/S0022112004002939).
- Nicoud, F., Baya Toda, H., Cabrit, O., Bose, S., and Lee, J. (2011). “Using singular values to build a subgrid-scale model for large eddy simulations”. In: *Phys. Fluids* 23, 085106. DOI: [10.1063/1.3623274](https://doi.org/10.1063/1.3623274).
- Nicoud, F. and Ducros, F. (1999). “Subgrid-scale stress modelling based on the square of the velocity gradient tensor”. In: *Flow Turbul. Combust.* 62, pp. 183–200. DOI: [10.1023/A:1009995426001](https://doi.org/10.1023/A:1009995426001).
- Oberlack, M. (1997). “Invariant modeling in large-eddy simulation of turbulence”. In: *Annual Research Briefs*, Center for Turbulence Research, Stanford University, pp. 3–22.
- Oberlack, M. (2001). “A unified approach for symmetries in plane parallel turbulent shear flows”. In: *J. Fluid Mech.* 427, pp. 299–328. DOI: [10.1017/S0022112000002408](https://doi.org/10.1017/S0022112000002408).
- Oberlack, M. (2002). “Symmetries and Invariant Solutions of Turbulent Flows and their Implications for Turbulence Modelling”. In: *Theories of Turbulence*. Ed. by Oberlack, M. and Busse, F. H. Vol. 442. International Centre for Mechanical Sciences. Springer Vienna, pp. 301–366. DOI: [10.1007/978-3-7091-2564-9_6](https://doi.org/10.1007/978-3-7091-2564-9_6).
- Pope, S. B. (1975). “A more general effective-viscosity hypothesis”. In: *J. Fluid Mech.* 72, pp. 331–340. DOI: [10.1017/S0022112075003382](https://doi.org/10.1017/S0022112075003382).
- Pope, S. B. (2011). *Turbulent Flows*. Cambridge: Cambridge University Press.
- Rasam, A., Brethouwer, G., Schlatter, P., Li, Q., and Johansson, A. V. (2011). “Effects of modelling, resolution and anisotropy of subgrid-scales on large eddy simulations of channel flow”. In: *J. Turbul.* 12, N10. DOI: [10.1080/14685248.2010.541920](https://doi.org/10.1080/14685248.2010.541920).
- Razafindralandy, D., Hamdouni, A., and Oberlack, M. (2007). “Analysis and development of subgrid turbulence models preserving the symmetry properties of the Navier–Stokes equations”. In: *Eur. J. Mech. B-Fluid.* 26, pp. 531–550. DOI: [10.1016/j.euromechflu.2006.10.003](https://doi.org/10.1016/j.euromechflu.2006.10.003).
- Remmerswaal, R. A. (2016). “A Family of Orthogonalised Nonlinear LES Models Based on the Velocity Gradient: Discretisation and Analysis”. Master’s thesis. University of Groningen, The Netherlands.
- Rivlin, R. S. (1955). “Further remarks on the stress-deformation relations for isotropic materials”. In: *J. Ration. Mech. Anal.* 4, pp. 681–702.
- Rivlin, R. S. and Ericksen, J. L. (1955). “Stress-deformation relations for isotropic materials”. In: *J. Ration. Mech. Anal.* 4, pp. 323–425.
- Rozema, W., Bae, H. J., Moin, P., and Verstappen, R. (2015). “Minimum-dissipation models for large-eddy simulation”. In: *Phys. Fluids* 27, 085107. DOI: [10.1063/1.4928700](https://doi.org/10.1063/1.4928700).
- Sagaut, P. (2006). *Large Eddy Simulation for Incompressible Flows. An Introduction*. 3rd ed. Springer-Verlag Berlin Heidelberg. DOI: [10.1007/b137536](https://doi.org/10.1007/b137536).
- Sagaut, P. and Cambon, C. (2018). *Homogeneous Turbulence Dynamics*. Springer, Cham. DOI: [10.1007/978-3-319-73162-9_7](https://doi.org/10.1007/978-3-319-73162-9_7).
- Sen, A., Mininni, P. D., Rosenberg, D., and Pouquet, A. (2012). “Anisotropy and nonuniversality in scaling laws of the large-scale energy spectrum in rotating turbulence”. In: *Phys. Rev. E* 86, 036319. DOI: [10.1103/PhysRevE.86.036319](https://doi.org/10.1103/PhysRevE.86.036319).
- Silvis, M. H., Remmerswaal, R. A., and Verstappen, R. (2017a). “A Framework for the Assessment and Creation of Subgrid-Scale Models for Large-Eddy Simulation”. In: *Progress in Turbulence VII: Proceedings of the iTi Conference in Turbulence 2016*. Ed. by Örlü, R., Talamelli, A., Oberlack, M., and Peinke, J. Springer International Publishing, pp. 133–139. DOI: [10.1007/978-3-319-57934-4_19](https://doi.org/10.1007/978-3-319-57934-4_19).
- Silvis, M. H., Remmerswaal, R. A., and Verstappen, R. (2017b). “Physical consistency of subgrid-scale models for large-eddy simulation of incompressible turbulent flows”. In: *Phys. Fluids* 29, 015105. DOI: [10.1063/1.4974093](https://doi.org/10.1063/1.4974093).

- Silvis, M. H., Trias, F. X., Abkar, M., Bae, H. J., Lozano-Durán, A., and Verstappen, R. W. C. P. (2016). “Exploring nonlinear subgrid-scale models and new characteristic length scales for large-eddy simulation”. In: *Studying Turbulence Using Numerical Simulation Databases - XVI: Proceedings of the 2016 Summer Program*. Ed. by Moin, P. and Urzay, J. Center for Turbulence Research, Stanford University, pp. 265–274.
- Silvis, M. H. and Verstappen, R. (2018). “Constructing Physically Consistent Subgrid-Scale Models for Large-Eddy Simulation of Incompressible Turbulent Flows”. In: *Turbulence and Interactions: Proceedings of the TI 2015 Conference*. Ed. by Deville, M. O., Couaillier, V., Estivalezes, J.-L., Gleize, V., Lê, T.-H., Terracol, M., and Vincent, S. Springer International Publishing, pp. 241–247. DOI: [10.1007/978-3-319-60387-2_26](https://doi.org/10.1007/978-3-319-60387-2_26).
- Silvis, M. H. and Verstappen, R. (2019). “Nonlinear Subgrid-Scale Models for Large-Eddy Simulation of Rotating Turbulent Flows”. In: *Direct and Large-Eddy Simulation XI*. Ed. by Salvetti, M. V., Armenio, V., Fröhlich, J., Geurts, B. J., and Kuerten, H. Springer International Publishing, pp. 129–134. DOI: [10.1007/978-3-030-04915-7_18](https://doi.org/10.1007/978-3-030-04915-7_18).
- Silvis, M. H. and Verstappen, R. (n.d.). “Creating physics-based turbulence models for large-eddy simulation”. (in preparation).
- Smagorinsky, J. (1963). “General circulation experiments with the primitive equations”. In: *Mon. Weather Rev.* 91, pp. 99–164. DOI: [10.1175/1520-0493\(1963\)091<0099:GCEWTP>2.3.CO;2](https://doi.org/10.1175/1520-0493(1963)091<0099:GCEWTP>2.3.CO;2).
- Smith, L. M. and Waleffe, F. (1999). “Transfer of energy to two-dimensional large scales in forced, rotating three-dimensional turbulence”. In: *Phys. Fluids* 11, pp. 1608–1622. DOI: [10.1063/1.870022](https://doi.org/10.1063/1.870022).
- Spencer, A. J. M. and Rivlin, R. S. (1958). “The theory of matrix polynomials and its application to the mechanics of isotropic continua”. In: *Arch. Ration. Mech. An.* 2, pp. 309–336.
- Spencer, A. J. M. and Rivlin, R. S. (1962). “Isotropic integrity bases for vectors and second-order tensors. Part I.” In: *Arch. Ration. Mech. An.* 9, pp. 45–63.
- Speziale, C. G. (1985). “Galilean invariance of subgrid-scale stress models in the large-eddy simulation of turbulence”. In: *J. Fluid Mech.* 156, pp. 55–62. DOI: [10.1017/S0022112085001987](https://doi.org/10.1017/S0022112085001987).
- Staplehurst, P. J., Davidson, P. A., and Dalziel, S. B. (2008). “Structure formation in homogeneous freely decaying rotating turbulence”. In: *J. Fluid Mech.* 598, pp. 81–105. DOI: [10.1017/S0022112007000067](https://doi.org/10.1017/S0022112007000067).
- Tafti, D. K. and Vanka, S. P. (1991). “A numerical study of the effects of spanwise rotation on turbulent channel flow”. In: *Phys. Fluids A* 3, pp. 642–656. DOI: [10.1063/1.858215](https://doi.org/10.1063/1.858215).
- Tao, B., Katz, J., and Meneveau, C. (2002). “Statistical geometry of subgrid-scale stresses determined from holographic particle image velocimetry measurements”. In: *J. Fluid Mech.* 457, pp. 35–78. DOI: [10.1017/S0022112001007443](https://doi.org/10.1017/S0022112001007443).
- Thiele, M. and Müller, W.-C. (2009). “Structure and decay of rotating homogeneous turbulence”. In: *J. Fluid Mech.* 637, pp. 425–442. DOI: [10.1017/S002211200999067X](https://doi.org/10.1017/S002211200999067X).
- Trias, F. X., Folch, D., Gorobets, A., and Oliva, A. (2015). “Building proper invariants for eddy-viscosity subgrid-scale models”. In: *Phys. Fluids* 27, 065103. DOI: [10.1063/1.4921817](https://doi.org/10.1063/1.4921817).
- Trias, F. X., Gorobets, A., Silvis, M. H., Verstappen, R. W. C. P., and Oliva, A. (2017). “A new subgrid characteristic length for turbulence simulations on anisotropic grids”. In: *Phys. Fluids* 29, 115109. DOI: [10.1063/1.5012546](https://doi.org/10.1063/1.5012546).
- Verstappen, R. (2011). “When Does Eddy Viscosity Damp Subfilter Scales Sufficiently?” In: *J. Sci. Comput.* 49, pp. 94–110. DOI: [10.1007/s10915-011-9504-4](https://doi.org/10.1007/s10915-011-9504-4).
- Verstappen, R. (2018). “How much eddy dissipation is needed to counterbalance the nonlinear production of small, unresolved scales in a large-eddy simulation of turbulence?” In: *Comput. Fluids* 176, pp. 276–284. DOI: [10.1016/j.compfluid.2016.12.016](https://doi.org/10.1016/j.compfluid.2016.12.016).
- Verstappen, R. W. C. P., Bose, S. T., Lee, J., Choi, H., and Moin, P. (2010). “A dynamic eddy-viscosity model based on the invariants of the rate-of-strain”. In: *Proceedings of the Summer Program*, Center for Turbulence Research, Stanford University, pp. 183–192.

- Verstappen, R. W. C. P., Rozema, W., and Bae, H. J. (2014). “Numerical scale separation in large-eddy simulation”. In: *Proceedings of the Summer Program*, Center for Turbulence Research, Stanford University, pp. 417–426.
- Verstappen, R. W. C. P. and Veldman, A. E. P. (2003). “Symmetry-preserving discretization of turbulent flow”. In: *J. Comput. Phys.* 187, pp. 343–368. DOI: [10.1016/S0021-9991\(03\)00126-8](https://doi.org/10.1016/S0021-9991(03)00126-8).
- Vreman, A. W. (2004). “An eddy-viscosity subgrid-scale model for turbulent shear flow: Algebraic theory and applications”. In: *Phys. Fluids* 16, pp. 3670–3681. DOI: [10.1063/1.1785131](https://doi.org/10.1063/1.1785131).
- Vreman, B., Geurts, B., and Kuerten, H. (1994a). “On the formulation of the dynamic mixed subgrid-scale model”. In: *Phys. Fluids* 6, pp. 4057–4059. DOI: [10.1063/1.868333](https://doi.org/10.1063/1.868333).
- Vreman, B., Geurts, B., and Kuerten, H. (1994b). “Realizability conditions for the turbulent stress tensor in large-eddy simulation”. In: *J. Fluid Mech.* 278, pp. 351–362. DOI: [10.1017/S0022112094003745](https://doi.org/10.1017/S0022112094003745).
- Vreman, B., Geurts, B., and Kuerten, H. (1996). “Large-Eddy Simulation of The Temporal Mixing Layer Using the Clark Model”. In: *Theor. Comp. Fluid Dyn.* 8, pp. 309–324. DOI: [10.1007/BF00639698](https://doi.org/10.1007/BF00639698).
- Vreman, B., Geurts, B., and Kuerten, H. (1997). “Large-eddy simulation of the turbulent mixing layer”. In: *J. Fluid Mech.* 339, pp. 357–390. DOI: [10.1017/S0022112097005429](https://doi.org/10.1017/S0022112097005429).
- Wang, B.-C. and Bergstrom, D. J. (2005). “A dynamic nonlinear subgrid-scale stress model”. In: *Phys. Fluids* 17, 035109. DOI: [10.1063/1.1858511](https://doi.org/10.1063/1.1858511).
- Wendling, I. and Oberlack, M. (2007). “On the Investigation of a Dynamic Nonlinear Subgrid-Scale Model”. In: *Complex Effects in Large Eddy Simulations*. Ed. by Kassinos, S. C., Langer, C. A., Iaccarino, G., and Moin, P. Springer Berlin Heidelberg, pp. 89–97. DOI: [10.1007/978-3-540-34234-2_7](https://doi.org/10.1007/978-3-540-34234-2_7).
- Winckelmans, G. S., Jeanmart, H., and Carati, D. (2002). “On the comparison of turbulence intensities from large-eddy simulation with those from experiment or direct numerical simulation”. In: *Phys. Fluids* 14, pp. 1809–1811. DOI: [10.1063/1.1466824](https://doi.org/10.1063/1.1466824).
- Winckelmans, G. S., Wray, A. A., Vasilyev, O. V., and Jeanmart, H. (2001). “Explicit-filtering large-eddy simulation using the tensor-diffusivity model supplemented by a dynamic Smagorinsky term”. In: *Phys. Fluids* 13, pp. 1385–1403. DOI: [10.1063/1.1360192](https://doi.org/10.1063/1.1360192).
- Xia, Z., Shi, Y., and Chen, S. (2016). “Direct numerical simulation of turbulent channel flow with spanwise rotation”. In: *J. Fluid Mech.* 788, pp. 42–56. DOI: [10.1017/jfm.2015.717](https://doi.org/10.1017/jfm.2015.717).
- Yang, Y.-T. and Wu, J.-Z. (2012). “Channel turbulence with spanwise rotation studied using helical wave decomposition”. In: *J. Fluid Mech.* 692, pp. 137–152. DOI: [10.1017/jfm.2011.500](https://doi.org/10.1017/jfm.2011.500).
- Yang, Z. X., Cui, G. X., Zhang, Z. S., and Xu, C. X. (2012a). “A modified nonlinear sub-grid scale model for large eddy simulation with application to rotating turbulent channel flows”. In: *Phys. Fluids* 24, 075113. DOI: [10.1063/1.4739063](https://doi.org/10.1063/1.4739063).
- Yang, Z., Cui, G., Xu, C., and Zhang, Z. (2012b). “Large eddy simulation of rotating turbulent channel flow with a new dynamic global-coefficient nonlinear subgrid stress model”. In: *J. Turbul.* 13, N48. DOI: [10.1080/14685248.2012.726996](https://doi.org/10.1080/14685248.2012.726996).
- Yeung, P. K. and Zhou, Y. (1998). “Numerical study of rotating turbulence with external forcing”. In: *Phys. Fluids* 10, pp. 2895–2909. DOI: [10.1063/1.869810](https://doi.org/10.1063/1.869810).
- Zang, Y., Street, R. L., and Koseff, J. R. (1993). “A dynamic mixed subgrid-scale model and its application to turbulent recirculating flows”. In: *Phys. Fluids A* 5, pp. 3186–3196. DOI: [10.1063/1.858675](https://doi.org/10.1063/1.858675).